Chapter 2
Quantum Theory of Gravitational-Wave Detectors

2.1 Preface

This chapter gives an overview of the quantum theory of gravitational-wave (GW) detectors. It is a modified version of the chapter contributed to a book in progress—*Advanced Gravitational-Wave Detectors*—edited by David Blair. This chapter is written by Yanbei Chen, and myself. It gives a detailed introduction on how to analyze the quantum noise in advanced GW detectors by using input–output formalism, which is also valid for general optomechanical devices. It discusses the origin of the Standard Quantum Limit (SQL) for GW sensitivity from both the dynamics of the optical field, and of the test-mass, which leads us to different approaches for surpassing the SQL: (i) creating correlations between the shot noise and back-action noise; (ii) modifying the dynamics of the test-mass, e.g., through the optical-spring effect; (iii) measuring the conserved dynamical quantity of the test-mass. For each of these approaches, the corresponding feasible configurations to achieve them are discussed in detail. This chapter presents the basic concepts and mathematical tools for understanding later chapters.

2.2 Introduction

The most difficult challenge in building a laser interferometer gravitational-wave (GW) detector is isolating the test masses from the rest of the world (e.g., random kicks from residual gas molecules, seismic activities, acoustic noises, thermal fluctuations, etc.), whilst keeping the device locked around the correct point of operation (e.g., pitch and yaw angles of the mirrors, locations of the beam spots, resonance condition of the cavities, and dark-port condition for the Michelson interferometer). Once all these issues have been solved, we arrive at the issue that we are going to analyze in this chapter: the fundamental noise that arises from quantum fluctuations in the system. A simple estimate, following the steps of Braginsky [2], will already lead

H. Miao, *Exploring Macroscopic Quantum Mechanics in Optomechanical Devices*, Springer Theses, DOI: 10.1007/978-3-642-25640-0_2,

us into the quantum world—as it will turn out, the superb sensitivity of GW detectors will be constrained by the back-action noise imposed by the *Heisenberg Uncertainty Principle*, when it is applied to test masses as heavy as 40 kg in the case of Advanced LIGO (AdvLIGO). As Braginsky realized in his analysis, there exists a *Standard Quantum Limit* (SQL) for the sensitivities of GW detectors—further improvements of detector sensitivity beyond this point require us to consider the application of techniques that manipulate the quantum coherence of light to our advantage. In this chapter, we will introduce a set of theoretical tools that will allow us to analyze GW detectors within the framework of quantum mechanics; using these tools, we will describe several examples in which the SQL can be surpassed.

The outline of this chapter is as follows: In Sect. 2.3, we will make an order-of-magnitude estimate of the quantum noise in a typical GW detector, from which we can gain a qualitative understanding of the origin of the SQL; then, in Sect. 2.4, we will introduce the basic concepts and tools to study the quantum dynamics of an interferometer, and the associated quantum noise. In Sect. 2.5, we will analyze the quantum noise in some simple systems to illustrate the procedures for implementing these tools—these simple systems are the fundamental building blocks for an advanced GW detector. We will start to study the quantum noise in a typical advanced GW detector in Sect. 2.6. We will increase the complexity step by step, each of which is connected in sequence to the simple systems analyzed in the previous section. Section 2.7 will present a rigorous derivation of the SQL from a more general context of linear continuous quantum measurements. This can enhance the understanding of the results in the previous section, and also pave the way to different approaches towards surpassing the SQL. In Sect. 2.8, we will talk about the first approach to surpassing the SQL by building correlations among quantum noises, and, in Sect. 2.9, we will illustrate the second approach to beating the SQL by modifying the dynamics of the test mass—in particular, we will discuss the optical spring effect to realize such an approach. Section 2.10 will present an alternative point of view on the origin of the SQL. This will introduce the idea of a speed meter as a third option for surpassing the SQL, in Sect. 2.11—two possible experimental configurations of the speed meter will be discussed. Finally, in Sect. 2.12, we will conclude with a summary of the main results in this chapter.

2.3 An Order-of-Magnitude Estimate

Here, we first make an order-of-magnitude estimate of the quantum limit for the sensitivity. We assume that test-masses have a reduced mass of m, and it is being measured by a laser beam with optical power I_0, and an angular frequency ω_0. Within a measurement duration τ, the number of photons is $N_\gamma = I_0\tau/(\hbar\omega_0)$. For a coherent light source (e.g., an ideal laser), the number of photons follows a Poisson distribution, and thus its root-mean-square fluctuation is $\sqrt{N_\gamma}$. The corresponding fractional error in the phase measurement, also called the *shot noise*, would be $\delta\phi_{\rm sh} = 1/\sqrt{N_\gamma}$. For detecting GWs with a period comparable to τ, the displacement

noise spectrum of the shot noise is:

$$S_{\rm sh}^x \approx \frac{\delta\phi_{\rm sh}^2}{k^2}\tau = \frac{\hbar c^2}{I_0\omega_0}, \tag{2.1}$$

with $k \equiv \omega_0/c$ as the wave number.

Meanwhile, the photon-number fluctuation also induces a random radiation-pressure force on the test-mass, which is the *radiation-pressure noise* (also called the back-action noise). Its magnitude is $\delta F_{\rm rp} = \sqrt{N_\gamma}\hbar k/\tau$, which is equal to the number fluctuation multiplied by the force of a single photon $\hbar k/\tau$. Since the response function of a free mass in the frequency domain is $-1/m\Omega^2$, the corresponding noise spectrum is:

$$S_{\rm rp}^x \approx \frac{\delta F_{\rm rp}^2}{m^2\Omega^4}\tau = \frac{I_0\omega_0}{c^2}\frac{\hbar}{m^2\Omega^4}. \tag{2.2}$$

The total noise spectrum is a sum of $S_{\rm sh}^x$ and $S_{\rm rp}^x$, namely:

$$S_{\rm tot}^x = S_{\rm sh}^x + S_{\rm rp}^x = \frac{\hbar c^2}{I_0\omega_0} + \frac{I_0\omega_0}{c^2}\frac{\hbar}{m^2\Omega^4} \geq \frac{2\hbar}{m\Omega^2}, \tag{2.3}$$

as illustrated in Fig. 2.1. The corresponding lower bound that does not depend on the optical power is $S_{\rm SQL}^x \equiv 2\hbar/(m\Omega^2)$. In terms of GW strain h, it reads

$$S_{\rm SQL}^h = \frac{1}{L^2}S_{\rm SQL}^x = \frac{2\hbar}{m\Omega^2L^2}, \tag{2.4}$$

with L being the arm length of the interferometer. This introduces us to the SQL [2, 3, 10], which arises as a trade-off between the shot noise and radiation-pressure noise. In the rest of this chapter, we will develop the necessary tools to analyze quantum noise of interferometers from first principles, and to derive the SQL more rigorously. This will allow us to design GW detectors that surpass this limit.

2.4 Basics for Analyzing Quantum Noise

To rigorously analyze the quantum noise in a detector, we need to study its quantum dynamics, of which the basics will be introduced in this section.

2.4.1 Quantization of the Optical Field and the Dynamics

For the optical field, the quantum operator of its quantized electric field is

$$\hat{E} = u(x,y,z)\int_0^{+\infty}\frac{d\omega}{2\pi}\sqrt{\frac{2\pi\hbar\omega}{\mathcal{A}c}}\left[\hat{a}_\omega e^{ikz-i\omega t} + \hat{a}_\omega^\dagger e^{+i\omega t-ikz}\right]. \tag{2.5}$$

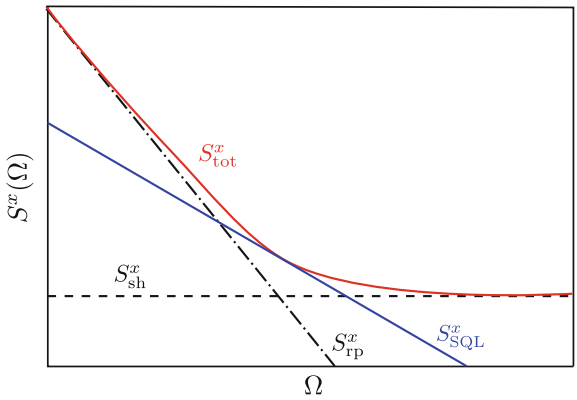

Fig. 2.1 A schematic plot of the displacement noise spectrum for a typical interferometer. Increasing or decreasing the optical power, the power-independent lower bound of the total spectrum will trace over the SQL

Here $\hat{a}^\dagger_\omega$ and $\hat{a}_\omega$ are the creation and annihilation operators, which satisfy $[\hat{a}_\omega,\ \hat{a}^\dagger_{\omega'}] = 2\pi\ \delta(\omega-\omega')$; $\mathcal{A}$ is the cross-sectional area of the optical beam; $u(x, y, z)$ is the spatial mode, satisfying $(1/\mathcal{A}) \int dxdy|u(x, y, z)|^2 = 1$.

For ground-based GW detectors, the GW signal that we are interested in is in the audio frequency range from 10 to 10^4 Hz. It creates sidebands on top of the carrier frequency of the laser ω_0 (3×10^{14} Hz). Therefore, it is convenient to introduce operators at these sideband frequencies to analyze the quantum noise. The upper and lower sideband operators are $\hat{a}_+ \equiv \hat{a}_{\omega_0+\Omega}$ and $\hat{a}_- \equiv \hat{a}_{\omega_0-\Omega}$, from which we can define the amplitude quadrature $\hat{a}_1$ and phase quadrature $\hat{a}_2$ as:

$$\hat{a}_1 = (\hat{a}_+ + \hat{a}^\dagger_-)/\sqrt{2}, \quad \hat{a}_2 = (\hat{a}_+ - \hat{a}^\dagger_-)/(i\sqrt{2}). \tag{2.6}$$

They coherently create one photon and annihilate one photon in the upper and lower sidebands, and this is, therefore, also called the two-photon formalism [9]. The electric field can then be rewritten as

$$\hat{E}(x, y, z, t) = u(x, y, z)\sqrt{\frac{4\pi\hbar\omega_0}{\mathcal{A}c}}\left[\hat{a}_1(z, t)\cos\omega_0 t + \hat{a}_2(z, t)\sin\omega_0 t\right].$$

where ω is approximated as ω_0 and the time-domain quadratures are defined as

$$\hat{a}_{1,2}(z, t) \equiv \int_0^{+\infty} \frac{d\Omega}{2\pi}\left(\hat{a}_{1,2}e^{-i\Omega t+ikz} + \hat{a}^\dagger_{1,2}e^{i\Omega t-ikz}\right). \tag{2.7}$$

These correspond to amplitude and phase modulations in the classical limit.[1]

After having introduced this quantization, we can look further at the dynamics of the optical field. The equations of motion that we will encounter turn out to be very

[1] To see such correspondence, suppose the electric field has a large steady-state amplitude A:

$$\hat{E}(z, t) = [A+\hat{a}_1(z, t)]\cos\omega_0 t+\hat{a}_2(z, t)\sin\omega_0 t \approx A\left[1 + \frac{\hat{a}_1(z, t)}{A}\right]\cos\left[\omega_0 t - \frac{\hat{a}_2(z, t)}{A}\right].$$

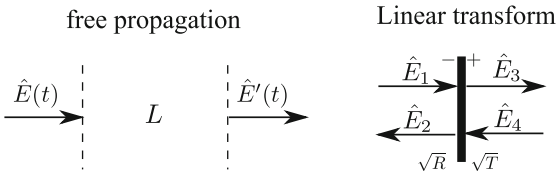

Fig. 2.2 Two basic dynamical processes of the optical field in analyzing the quantum noise of an interferometer

simple, and only two are relevant, as shown in Fig. 2.2: (i) *A free propagation.* Given a free propagation distance of L, the new field $\hat{E}'(t)$ is

$$\hat{E}'(t) = \hat{E}(t-\tau), \tag{2.8}$$

with $\tau \equiv L/c$; (ii) *Continuity condition on the mirror surface.*

$$\hat{E}_2(t) = \sqrt{T}\hat{E}_4(t) - \sqrt{R}\hat{E}_1(t), \tag{2.9}$$

$$\hat{E}_3(t) = \sqrt{R}\hat{E}_4(t) + \sqrt{T}\hat{E}_1(t), \tag{2.10}$$

with transmissivity T, reflectivity R, and a sign of convention as indicated in the figure. These equations relate the optical field before and after the mirror. Due to the linearity of this system, they are both identical to the classical equations of motion.

In later discussions, different quantities of the optical field will always be compared at the same location, and they will all share the same spatial mode. In addition, the propagation phase shift can be absorbed into the time delay. Therefore, we will ignore the factors $u(x, y, z)\sqrt{\frac{4\pi\hbar\omega_0}{\mathcal{A}c}}$, and $e^{\pm ikz}$, hereafter.

2.4.2 Quantum States of the Optical Field

To determine the expectation value and the quantum fluctuation of the Heisenberg operators (related to the quantum noise), e.g., $\langle\psi|\hat{O}|\psi\rangle$, not only should we specify the evolution of $\hat{O}$, but we also need to specify the quantum state $|\psi\rangle$. Of particular interest to us are vacuum, coherent, and squeezed states.

Vacuum state—The vacuum state $|0\rangle$ is, by definition, the state with no excitation and for every frequency, $\hat{a}_\Omega|0\rangle = 0$. The associated fluctuation is:

$$\langle 0|\hat{a}_i(\Omega)\hat{a}_j^\dagger(\Omega')|0\rangle_{\text{sym}} = \pi\delta_{ij}\delta(\Omega-\Omega'), \ \ (i, j = 1, 2). \tag{2.11}$$

Equivalently, the double-sided spectral densities [2] for $\hat{a}_{1,2}$ are

[2] For any pair of operators $\hat{O}_1$ and $\hat{O}_2$, the double-sided spectral density is defined through

$$\frac{1}{2\pi}\langle 0|\hat{O}_1(\Omega')\hat{O}_2^\dagger(\Omega)|0\rangle_{\text{sym}} \equiv \frac{1}{2\pi}\langle 0|\hat{O}_1(\Omega')\hat{O}_2^\dagger(\Omega)+\hat{O}_2^\dagger(\Omega)\hat{O}_1(\Omega')|0\rangle \equiv \frac{1}{2}S_{O_1O_2}(\Omega)\delta(\Omega-\Omega').$$

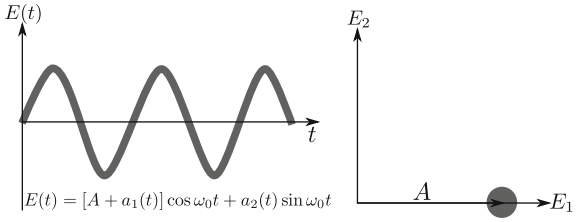

Fig. 2.3 A schematic plot of the electric field and the fluctuations of amplitude and phase quadrature (*shaded area*). The *left* panel shows the time evolution of E, and the *right* panel shows E in the space expanded by the amplitude and phase quadratures (E_1, E_2)

$$S_{a_1}(\Omega) = S_{a_2}(\Omega) = 1, \quad S_{a_1 a_2}(\Omega) = 0. \tag{2.12}$$

Coherent state—The coherent state is defined by [1] as:

$$|\alpha\rangle \equiv \hat{D}[\alpha]|0\rangle \equiv \exp\left[\int \frac{d\Omega}{2\pi}(\alpha_\Omega \hat{a}_\Omega^\dagger - \alpha_\Omega^* \hat{a}_\Omega)\right]|0\rangle, \tag{2.13}$$

which satisfies $\hat{a}_{\Omega'}|\alpha\rangle = \alpha(\Omega')\,|\alpha\rangle$. The operator $\hat{D}$ is unitary, so $\hat{D}^\dagger \hat{D} = \hat{I}$. We can use this to make a unitary transformation for studying the problem

$$|\psi\rangle \to \hat{D}^\dagger|\psi\rangle, \quad \hat{O} \to \hat{D}^\dagger \hat{O}\,\hat{D}, \tag{2.14}$$

which leaves the physics invariant. This means that the coherent state can be replaced by the vacuum state, as long as we perform corresponding transformations of $\hat{O}$ into $\hat{D}^\dagger \hat{O}\,\hat{D}$. For the annihilation and creation operators, we have $\hat{D}^\dagger(\alpha)\hat{a}_\Omega \hat{D}(\alpha) = \hat{a}_\Omega + \alpha_\Omega$ and $\hat{D}^\dagger(\alpha)\hat{a}_\Omega^\dagger \hat{D}(\alpha) = \hat{a}_\Omega^\dagger + \alpha_\Omega^*$, i.e., the original operators plus some complex constants.

An ideal single-mode laser with a central frequency ω_0 can be modeled as a coherent state, and $\alpha_\Omega = \pi\,\bar{a}\,\delta(\Omega - \omega_0)$, with $\bar{a} = \sqrt{2I_0/(\hbar\,\omega_0)}$ and I_0 is the optical power. Under transformation $\hat{D}$, the electric field reads [cf. Eq. (2.7)]:

$$\hat{E}(t) = [\bar{a} + \hat{a}_1(t)]\cos\omega_0 t + \hat{a}_2(t)\sin\omega_0 t, \tag{2.15}$$

which is simply a sum of a classical amplitude and quantum quadrature fields. This is what we intuitively expect for the optical field from a single-mode laser, namely "quantum fluctuations" superimposed onto a "classical carrier". In Fig. 2.3, we show $E(t)$ and the associated fluctuations in the amplitude and phase quadratures schematically. As we will see later, these fluctuations are attributable to the quantum noise and the associated SQL.

Squeezed state—A more complicated state would be the squeezed state:

$$|[\chi]\rangle \equiv \exp\left[\int_0^{+\infty} \frac{d\Omega}{2\pi}\left(\chi_\Omega\,\hat{a}_+^\dagger \hat{a}_-^\dagger - \chi_\Omega^*\,\hat{a}_+ \hat{a}_-\right)\right]|0\rangle \equiv \hat{S}[\chi]|0\rangle. \tag{2.16}$$

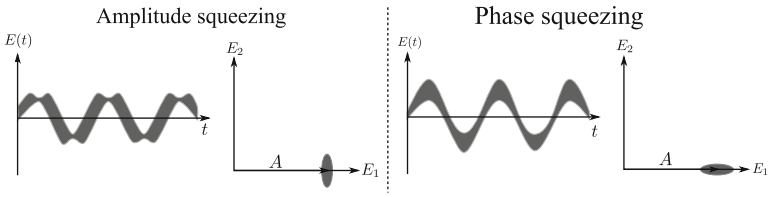

Fig. 2.4 The fluctuations of the amplitude and phase quadratures (*shaded areas*) of the squeezed state. The *left* two panels show the case of amplitude squeezing; the *right* two panels show the phase squeezing

Similar to the coherent-state case, we can also better understand a squeezed state by making a unitary transformation of the basis through $\hat{S}$. By redefining $\chi_\Omega \equiv \xi_\Omega\, e^{-2i\phi_\Omega}$ ($\xi_\Omega, \phi_\Omega \in \Re$), for quadratures, this leads to:

$$\hat{S}^\dagger \hat{a}_1 \hat{S} = \hat{a}_1(\cosh\xi + \sinh\xi\cos 2\phi) - \hat{a}_2 \sinh\xi \sin 2\phi, \tag{2.17}$$

$$\hat{S}^\dagger \hat{a}_2 \hat{S} = \hat{a}_2(\cosh\xi - \sinh\xi\cos 2\phi) - \hat{a}_1 \sinh\xi \sin 2\phi. \tag{2.18}$$

Let us look at two special cases: (1) $\phi = \pi/2$. We have

$$\hat{S}^\dagger \hat{a}_1 \hat{S} = e^{-\xi}\hat{a}_1, \quad \hat{S}^\dagger \hat{a}_2 \hat{S} = e^{\xi}\hat{a}_2, \tag{2.19}$$

in which the amplitude quadrature fluctuation is squeezed by $e^{-\xi}$ while the phase quadrature is magnified by e^{ξ}; (2) $\phi = 0$. The situation will just be the opposite. Both cases are shown schematically in Fig. 2.4.

2.4.3 Dynamics of the Test-Mass

Similarly, due to the linear dynamics, the quantum equations of motion for the test masses (relative motion) are formally identical to their classical counterparts:

$$\dot{\hat{x}}(t) = \hat{p}(t)/m, \quad \dot{\hat{p}}(t) = \hat{I}(t)/c + mL\ddot{h}(t). \tag{2.20}$$

Here $\hat{x}$ and $\hat{p}$ are the position and momentum operators, which satisfy $[\hat{x},\ \hat{p}] = i\hbar$; $\hat{I}(t)/c$ is the radiation pressure, which is a linear function of the optical quadrature fluctuations; $mL\ddot{h}(t)$ is the GW tidal force. Since the detection frequency ($\sim$100 Hz) is much larger than the pendulum frequency ($\sim$1 Hz) of the test-masses in a typical detector, they are treated as free masses.

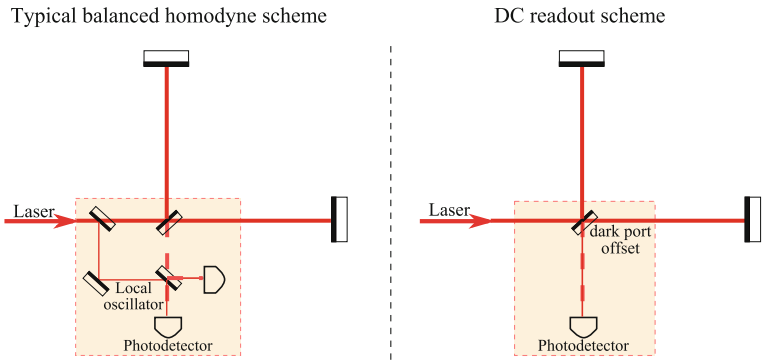

Fig. 2.5 A schematic plot of two homodyne readout schemes

2.4.4 Homodyne Detection

In this section, we will consider how to detect the phase shift of the output optical field which contains the GW signal. To make a phase sensitive measurement, we need to measure the quadratures of the optical field, instead of its power. This can be achieved by a *homodyne detection* in which the output signal light is mixed with a *local oscillator*, thus producing a photon flux that depends linearly on the phase (i.e., on the GW strain). Specifically, for a local oscillator $L(t) = L_1 \cos\omega_0 t + L_2 \sin\omega_0 t$ and output $\hat{b}(t) = \hat{b}_1(t)\cos\omega_0 t + \hat{b}_2(t)\sin\omega_0 t$, the photocurrent is $i(t) \propto |L(t) + \hat{b}(t)|^2 = 2L_1\hat{b}_1(t) + 2L_2\hat{b}_2(t) + \cdots$. The rest of the terms, represented by "$\cdots$", contain either frequency components that are strictly DC and around $2\omega_0$, and terms quadratic in $\hat{b}$. In such a way, we can measure a given quadrature $\hat{b}_\zeta(t) = \hat{b}_1(t)\cos\zeta + \hat{b}_2(t)\sin\zeta$, by choosing the correct local oscillator, such that $\tan\zeta = L_2/L_1$.

In order to realize the above ideal superposition, there are two possible schemes: introducing the local oscillator from the injected laser (external scheme as shown in the right panel of Fig. 2.5;) or intentionally offsetting the two arms at the very beginning, with a very small phase mismatch, which results in the so-called DC readout scheme, as shown in the left panel of Fig. 2.5.

2.5 Examples

Before analyzing the quantum noise in an advanced interferometric GW detector, it is illustrative to first consider three examples: (1) A test mass coupled to an optical field in free space; (2) A tuned Fabry-Pérot cavity with a movable end mirror as the test mass; (3) A detuned Fabry-Pérot cavity with a movable end mirror. These three examples summarize the main physical processes in an advanced GW detector. Understanding them will not only help us to get familiar with the tools for analyzing

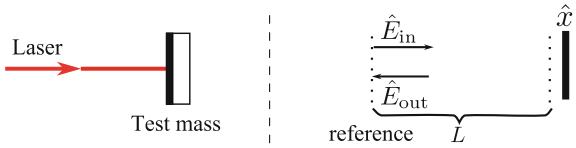

Fig. 2.6 A schematic plot of the interaction between the test mass and a coherent optical field in free space (*left*); and the associated physical quantities (*right*)

quantum noise in a GW detector, but can also provide intuitive pictures which will be useful in understanding more complicated configurations.

2.5.1 Example I: Free Space

The model is shown schematically in Fig. 2.6. The laser-pumped input optical field can be written as [cf. Eq. (2.15)]:

$$\hat{E}_{\rm in}(t) = \left[\sqrt{2I_0/(\hbar\omega_0)} + \hat{a}_1(t)\right]\cos\omega_0 t + \hat{a}_2(t)\sin\omega_0 t. \tag{2.21}$$

The output field $\hat{E}_{\rm out}(t)$ is simply:

$$\hat{E}_{\rm out}(t) = \hat{E}_{\rm in}(t - 2\tau - 2\hat{x}/c), \tag{2.22}$$

with a delay time $\tau \equiv L/c$. We define output quadratures $\hat{b}_1$ and $\hat{b}_2$ through:

$$\hat{E}_{\rm out}(t) = \left[\sqrt{2I_0/(\hbar\omega_0)} + \hat{b}_1(t)\right]\cos\omega_0 t + \hat{b}_2(t)\sin\omega_0 t. \tag{2.23}$$

Since the displacement of the test mass is small, and the uncertainty of $\omega_0\hat{x}/c$ is much smaller than unity, we can make a Taylor expansion of Eq. (2.22) in a series of $\omega_0\hat{x}/c$. Up to the leading order, we obtain the following input–output relations:

$$\hat{b}_1(t) = \hat{a}_1(t - 2\tau), \tag{2.24}$$

$$\hat{b}_2(t) = \hat{a}_2(t - 2\tau) - 2\sqrt{\frac{2I_0}{\hbar\omega_0}}\frac{\omega_0}{c}\hat{x}(t - \tau), \tag{2.25}$$

where, for simplicity, we have assumed that $\omega_0 L/c = n\,\pi$, with n an integer.

The equation of motion for the test-mass displacement $\hat{x}$ is simply:

$$m\ddot{\hat{x}}(t) = \hat{F}_{\rm rp}(t) + \frac{1}{2}mL\ddot{h}(t). \tag{2.26}$$

Here we have chosen an inertial reference frame, as indicated in Fig. 2.6, such that the gravitational tidal force is equal to $\frac{1}{2}mL\ddot{h}(t)$; the radiation-pressure force $\hat{F}_{\rm rp}$ on the test-mass is given by:

$$\hat{F}_{\rm rp}(t) = 2\frac{\mathcal{A}}{4\pi}\overline{|\hat{E}_{\rm in}(t-\tau)|^2} = 2\frac{I_0}{c}\left[1+\sqrt{\frac{2\hbar\omega_0}{I_0}}\hat{a}_1(t-\tau)\right], \tag{2.27}$$

where in the second equality we have kept to the first order of the amplitude quadrature. There is a DC component in the radiation-pressure force, which can be balanced in the experiment (e.g., by the wire tension in the case of a suspended pendulum). We are interested in the perturbed part, proportional to the amplitude quadrature, which accounts for the radiation-pressure noise.

We can solve Eqs. (2.24), (2.25) and (2.26) by transforming them into the frequency domain, after which we obtain:

$$\vec{b}(\Omega) = \mathbf{M}\,\vec{a}(\Omega) + \vec{D}\,h(\Omega), \tag{2.28}$$

where $\vec{a} = (\hat{a}_1, \hat{a}_2)^{\mathbf{T}}$, $\vec{b} = (\hat{b}_1, \hat{b}_2)^{\mathbf{T}}$ (superscript $^{\mathbf{T}}$ denoting transpose); the transfer matrix $\mathbf{M}$ and transfer vector $\vec{D}$ can be read off from the following explicit expression of Eq. (2.28):

$$\begin{bmatrix}\hat{b}_1(\Omega)\\ \hat{b}_2(\Omega)\end{bmatrix} = e^{2i\Omega\tau}\begin{bmatrix}1 & 0\\ -\kappa & 1\end{bmatrix}\begin{bmatrix}\hat{a}_1(\Omega)\\ \hat{a}_2(\Omega)\end{bmatrix} + \begin{bmatrix}0\\ e^{i\Omega\tau}\sqrt{2\kappa}\end{bmatrix}\frac{h(\Omega)}{h_{\rm SQL}}, \tag{2.29}$$

with

$$\kappa = \frac{8I_0\omega_0}{mc^2\Omega^2}, \quad h_{\rm SQL} = \sqrt{\frac{8\hbar}{m\Omega^2L^2}}. \tag{2.30}$$

As we can see, the GW signal is contained in the output phase quadrature $\hat{b}_2$. It can be decomposed into signal and noise components:

$$\hat{b}_2(\Omega) = \langle\hat{b}_2(\Omega)\rangle + \Delta\hat{b}_2(\Omega), \tag{2.31}$$

where $\langle\hat{b}_2(\Omega)\rangle$ is the expectation value of the output, which is proportional to the GW signal h, and Δb_2 is the quantum fluctuation with zero expectation. By defining $\langle\hat{b}_2(\Omega)\rangle \equiv \mathcal{T}h$, we introduce the following quantity:

$$\mathcal{T} = e^{i\Omega\tau}\sqrt{2\kappa}\frac{1}{h_{\rm SQL}}, \tag{2.32}$$

which is the transfer function from the GW strain h to the output phase quadrature. This particular form indicates that the output phase modulation is proportional to the GW strain, delayed by a constant time τ. The noise part

$$\Delta\hat{b}_2(\Omega) = e^{2i\Omega\tau}\hat{a}_2(\Omega) - e^{2i\Omega\tau}\kappa\,\hat{a}_1(\Omega), \tag{2.33}$$

contains two parts: (i) the first one is the *shot noise* $\hat{n}_{\rm sh} \equiv e^{2i\Omega\tau}\hat{a}_2$, which arises from the phase-quadrature fluctuation of the input optical field and has a flat spectrum [cf. Eq. (2.12)]:

$$S_{\rm sh}(\Omega) = 1; \tag{2.34}$$

and (ii) the second one is the *radiation-pressure noise* $\hat{n}_{\rm rp} \equiv (-e^{2i\Omega\tau}\kappa\,\hat{a}_1)$. This arises from the amplitude-quadrature fluctuation, and has the following noise spectrum:

$$S_{\rm rp}(\Omega) = \kappa^2, \tag{2.35}$$

with a frequency dependence of $1/\Omega^4$.

Given the coherent state of the input optical field, the amplitude and phase-quadrature fluctuations are not correlated. Therefore, we can obtain the total noise spectrum simply by summing up $S_{\rm sh}$ and $S_{\rm rp}$. By normalizing with the transfer function $\mathcal{T}$, the signal-referred noise spectrum can be written as:

$$S^h(\Omega) = \frac{1}{|\mathcal{T}|^2} S_{\Delta\hat{b}_2}(\Omega) = \left[\frac{1}{\kappa} + \kappa\right] \frac{h^2_{\rm SQL}}{2} \geq h^2_{\rm SQL}. \tag{2.36}$$

The shot-noise contribution (first term) is inversely proportional to the optical power ($\kappa \propto I_0$) and the radiation-pressure noise (second term) is proportional to I_0. The balance between them gives the SQL for detecting GWs with this simple model. We will find that although this model is simple, it summarizes the main features of a GW detector.

2.5.2 Example II: A Tuned Fabry-Pérot Cavity

Now we consider the case of a tuned Fabry-Pérot cavity. In Fig. 2.7, we show the model schematically. In comparison with the previous case, an additional mirror with transmissivity (of power) T, and reflectivity R, are placed in front of the test-mass, in effect "wrapping" around the original system. We define the new input and output optical fields $\hat{E}'_{\rm in,out}$, in a similar way to that of $\hat{E}_{\rm in,out}$, by simply replacing $\vec{a}, \vec{b}$ with new amplitude and phase quadratures $\vec{\alpha}, \vec{\beta}$. We need to determine a new input–output relation between $\hat{\alpha}_{1,2}$ and $\hat{\beta}_{1,2}$. From the continuity condition on the front mirror surface (cf. Eqs. (2.9) and (2.10), we have:

$$\hat{E}_{\rm in} = \sqrt{R}\hat{E}_{\rm out} + \sqrt{T}\hat{E}'_{\rm in}, \tag{2.37}$$

$$\hat{E}'_{\rm out} = \sqrt{T}\hat{E}_{\rm out} - \sqrt{R}\hat{E}'_{\rm in}. \tag{2.38}$$

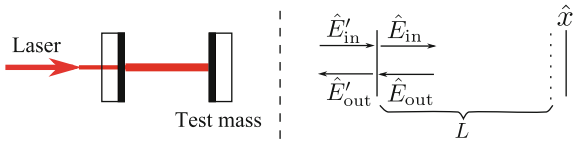

Fig. 2.7 A schematic plot of the tuned-cavity model (*left*); and the associated physical quantities (*right*)

Correspondingly, $\vec{a}, \vec{b}$ are related to new quadrature fields $\vec{\alpha}, \vec{\beta}$ by:

$$\vec{a} = \sqrt{R}\,\vec{b} + \sqrt{T}\,\vec{\alpha}, \tag{2.39}$$

$$\vec{\beta} = \sqrt{T}\,\vec{b} - \sqrt{R}\,\vec{\alpha}. \tag{2.40}$$

Together with Eq. (2.28), it would be straightforward to obtain the new input–output relation. Generally, the expression is rather cumbersome. We will focus on the case in which the transmissivity T is small (i.e., a high-finesse cavity). In addition, since the GW sideband frequency Ω we are interested in is around 100 Hz, $\Omega\,\tau$ is much smaller than unity even when the cavity length L is 4 km. Therefore, we can make a Taylor expansion of the new input–output relation as a series of the dimensionless quantities T and $\Omega\,\tau$. Up to the leading order, this leads to:

$$\begin{bmatrix} \hat{\beta}_1(\Omega) \\ \hat{\beta}_2(\Omega) \end{bmatrix} = e^{2i\phi} \begin{bmatrix} 1 & 0 \\ -\mathcal{K} & 1 \end{bmatrix} \begin{bmatrix} \hat{\alpha}_1(\Omega) \\ \hat{\alpha}_2(\Omega) \end{bmatrix} + e^{-i\phi} \begin{bmatrix} 0 \\ \sqrt{2\mathcal{K}} \end{bmatrix} \frac{h}{h_{\rm SQL}}. \tag{2.41}$$

We have introduced:

$$\phi \equiv \arctan(\Omega/\gamma), \quad \mathcal{K} \equiv \frac{2\gamma\,\iota_c}{\Omega^2(\Omega^2+\gamma^2)}, \tag{2.42}$$

with the cavity bandwidth $\gamma \equiv Tc/(4L)$, parameter $\iota_c \equiv 8\omega_0 I_c/(mLc)$, and intracavity power $I_c \equiv 4I_0/T$.

The same as the previous free-space case, we need to read out the phase quadrature of the output field which contains the GW signal. The corresponding *signal-referred* noise spectrum S^h has a similar form to the previous free-space case, but with κ replaced by $\mathcal{K}$ [cf. Eq. (2.36)], i.e.:

$$S^h(\Omega) = \left[\frac{1}{\mathcal{K}} + \mathcal{K}\right] \frac{h_{\rm SQL}^2}{2} \geq h_{\rm SQL}^2. \tag{2.43}$$

For frequencies around $\Omega \sim \gamma$, the shot noise spectrum almost decreases by a factor of $1/T^2$ in comparison with the free-space case. This is attributable to the coherent amplification of the optical power and the signal. The additional mirror serves as a quantum feedback, which allows signals to build up coherently, whilst noise adds up incoherently over time (On the other hand, a classical feedback will not normally increase the signal-to-noise ratio, as feeding back what is already known will not increase knowledge.). For frequencies $\Omega > \gamma$, the shot noise increases as Ω^2, rather than remaining constant in the previous case. This is due to the non-zero response time of the cavity, and signal with frequencies higher than γ are averaged out. Therefore, the cavity bandwidth roughly determines the detection bandwidth.

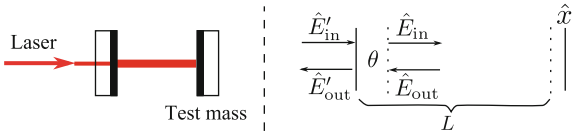

Fig. 2.8 A schematic plot of a detuned cavity; and the associated physical quantities (*right*). Here, θ is the detuned phase

2.5.3 Example III: A Detuned Fabry-Pérot Cavity

If the cavity is not tuned, as shown schematically in Fig. 2.8, namely, $\omega_0\tau = \theta + n\pi$ ($\theta \neq 0$) with n an integer, the free propagation will not only induce a phase shift, but also a rotation of the quadratures. This simply arises from the following fact: given a free-space propagation of τ, and from the relation $\hat{E}^{\rm out}(t) = \hat{E}^{\rm in}(t-\tau)$, the quadrature evolves as:

$$\begin{bmatrix} \hat{b}_1(\Omega) \\ \hat{b}_2(\Omega) \end{bmatrix} = e^{i\Omega\tau} \begin{bmatrix} \cos\omega_0\tau & -\sin\omega_0\tau \\ \sin\omega_0\tau & \cos\omega_0\tau \end{bmatrix} \begin{bmatrix} \hat{a}_1(\Omega) \\ \hat{a}_2(\Omega) \end{bmatrix}, \tag{2.44}$$

which is a delay and rotation.

Correspondingly, Eqs. (2.39) and (2.40) are modified:

$$\vec{a} = \sqrt{R}\,\mathbf{R}_{2\theta}\,\vec{b} + \sqrt{T}\,\mathbf{R}_{\theta}\,\vec{\alpha}, \tag{2.45}$$

$$\vec{\beta} = \sqrt{T}\,\mathbf{R}_{\theta}\,\vec{b} - \sqrt{R}\,\vec{\alpha}, \tag{2.46}$$

where $\mathbf{R}_\theta$ is the rotation matrix, defined as

$$\mathbf{R}_\theta \equiv \begin{pmatrix} \cos\theta & -\sin\theta \\ \sin\theta & \cos\theta \end{pmatrix}. \tag{2.47}$$

Similarly, if the detuned phase is small, with $\theta \ll 1$, we can make a Taylor expansion of these equations in series of θ, T and $\Omega\,\tau$. After some manipulation, the new input–output relation can be expressed in the following compact form:

$$\vec{\beta}(\Omega) = \frac{1}{\mathcal{C}}[\mathbf{M}\,\vec{\alpha}(\Omega) + \vec{D}\,h(\Omega)], \tag{2.48}$$

where

$$\mathcal{C} = \Omega^2[(\Omega + i\gamma)^2 - \Delta^2] + \Delta\iota_c, \tag{2.49}$$

$$\mathbf{M} = \begin{bmatrix} -\Omega^2(\Omega^2 + \gamma^2 - \Delta^2) - \Delta\,\iota_c & 2\gamma\,\Delta\Omega^2 \\ -2\gamma\,\Delta\Omega^2 + 2\gamma\iota_c & -\Omega^2(\Omega^2 + \gamma^2 - \Delta^2) - \Delta\iota_c \end{bmatrix}, \tag{2.50}$$

$$\vec{D} = \begin{bmatrix} \Delta\Omega \\ (-\gamma + i\Omega)\Omega \end{bmatrix} \frac{2\sqrt{\gamma\iota_c}}{h_{\rm SQL}}, \tag{2.51}$$

with detuning frequency $\Delta \equiv \theta/\tau$. Here we have ignored the tiny frequency-dependent phase correction $\Omega\,\theta/\omega_0$. Unlike in the previous two cases, the GW signal here appears in both amplitude and phase quadratures. To readout the GW signal, we can make a homodyne detection of a certain output quadrature:

$$\hat{\beta}_\zeta(\Omega) = \hat{\beta}_1(\Omega)\cos\zeta + \hat{\beta}_2(\Omega)\sin\zeta. \tag{2.52}$$

Given a coherent state input, the corresponding signal-referred noise spectrum density is

$$S^h(\Omega) = \frac{(\cos\zeta,\ \sin\zeta)\mathbf{M}\mathbf{M}^{\mathbf{T}}(\cos\zeta,\ \sin\zeta)^{\mathbf{T}}}{|D_1\cos\zeta + D_2\sin\zeta|^2}, \tag{2.53}$$

with $D_{1,2}$ being the components of the vector $\vec{D}$. This expression recovers the previous two cases: (1) the tuned cavity, by setting $\Delta = 0$, and phase quadrature measurement $\zeta = 0$; (2) the free-space case, by setting the cavity bandwidth $\gamma \to \infty$. We will postpone discussing the physical significance of this formula until we consider a signal-recycled GW detector, which can actually be mapped into a detuned Fabry-Pérot cavity.

2.6 Quantum Noise in an Advanced GW Detector

After having introduced some basic principles and examples, we are now ready to analyze the quantum noise of a typical advanced GW detector: a Michelson interferometer with Fabry-Pérot arm cavities, a power-recycling mirror (PRM), and a signal-recycling mirror (SRM). This is shown schematically in Fig. 2.9.

To make a direct one-to-one correspondence between the input–output relation of an advanced GW detector and the three examples we have considered, we will gradually introduce important optical elements, and discuss them in the following sequence: (1) a simple Michelson interferometer with only end test-masses (Sect. 2.6.1); (2) a power-recycled interferometer with both power-recycling mirror and arm cavities (Sect. 2.6.2); (3) a power- and signal-recycled interferometer (Sect. 2.6.3).

2.6.1 Input–Output Relation of a Simple Michelson Interferometer

A simple Michelson interferometer is shown schematically in Fig. 2.10. Ideally, the interferometer is set up to have identical arms, so that at the zero working point of the

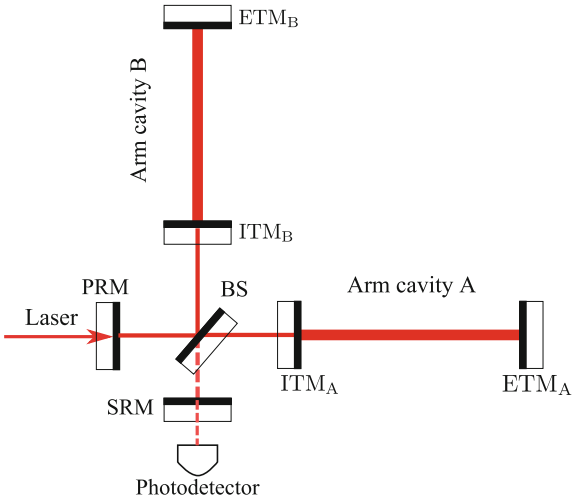

Fig. 2.9 A schematic plot of an advanced GW detector. The beam splitter (*BS*) splits the laser light into two beams. The internal test-mass (*ITM*) and end test-mass (*ETM*) with optical coatings on their surface form the Fabry-Pérot arm cavities which amplifies both the signal and optical power. The power recycling mirror (*PRM*) can further increase the circulating power. The signal-recycling mirror (*SRM*) folds the signal back into the interferometer, and it significantly enriches the dynamics of the system, as discussed in the main text

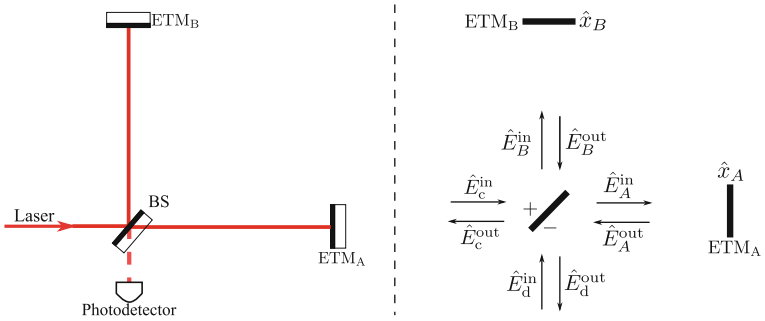

Fig. 2.10 A schematic plot of a simple Michelson interferometer (*left*); and its mathematical model with propagating optical fields (*right*)

interferometer (i.e., when locked on a dark fringe), fields entering from each port will only return to that port. The carrier light enters and exits from the *common* (*bright*) *port*, while the differential port remains *dark*. The differential motion of the test mass $\hat{x}_A - \hat{x}_B$, which contains the GW signal causes a differential phase modulation, and therefore induces an output signal out of the differential (dark) port, at which we make homodyne detections.

We follow steps similar to those in Sect. 2.5.1 to derive the input–output relation here. As we will see, the input–output relation of the differential displacement

we are interested in is exactly the same as the free-space scenario considered in Sect. 2.5.1. The laser-pumped input optical field into the common port is:

$$\hat{E}_{\rm c}^{\rm in}(t) = [\sqrt{2I_0/(\hbar\omega_0)} + \hat{c}_1(t)]\cos\omega_0 t + \hat{c}_2(t)\sin\omega_0 t. \tag{2.54}$$

With no laser pumping, the input field into the differential port is simply:

$$\hat{E}_{\rm d}^{\rm in}(t) = \left[\hat{a}_1(t)\cos\omega_0 t + \hat{a}_2(t)\sin\omega_0 t\right]. \tag{2.55}$$

The fields, after passing through the half-half beam splitter, and while propagating towards $\mathrm{ETM_A}$ and $\mathrm{ETM_B}$, are:

$$\hat{E}_{A,B}^{\rm in}(t) = \frac{\hat{E}_{\rm c}^{\rm in}(t) \mp \hat{E}_{\rm d}^{\rm in}(t)}{\sqrt{2}}. \tag{2.56}$$

The fields returning from the ETM are

$$\hat{E}_{A,B}^{\rm out}(t) = \hat{E}_{A,B}^{\rm in}(t - 2\tau - 2\hat{x}_{A,B}/c), \tag{2.57}$$

where $\tau \equiv L/c$ is the time for light to propagate from the beam splitter to each of the ETMs. To the leading order in $\hat{x}_{A,B}$, we have:

$$\hat{E}_{\rm d}^{\rm out}(t) = \frac{\hat{E}_B^{\rm out}(t) - \hat{E}_A^{\rm out}(t)}{\sqrt{2}} \equiv [\hat{b}_1(t)\cos\omega_0 t + \hat{b}_2(t)\sin\omega_0 t], \tag{2.58}$$

with

$$\hat{b}_1(t) = \hat{a}_1(t - 2\tau), \tag{2.59}$$

$$\hat{b}_2(t) = \hat{a}_2(t - 2\tau) - \sqrt{\frac{2I_0}{\hbar\omega_0}}\frac{\omega_0}{c}\hat{x}_d(t - \tau), \tag{2.60}$$

where we have assumed $\omega_0 L/c = n\pi$, with n an integer; and have defined the differential-mode motion:

$$\hat{x}_d(t) \equiv \hat{x}_B(t) - \hat{x}_A(t). \tag{2.61}$$

Radiation-pressure forces acting on the two test-masses have both common and differential components, which are proportional to $\hat{c}_1$ and $\hat{a}_1$ respectively. If test masses have nearly the same mass, m, then $\hat{c}_1$ ($\hat{a}_1$) will only induce common-mode (differential-mode) motion. Mathematically, we have, up to leading order in fluctuations/modulations:

$$\hat{F}_{A,B}(t) = 2\frac{I_0}{c}\left[1 + \sqrt{\frac{\hbar\omega_0}{I_0}}\frac{\hat{c}_1(t - \tau) \mp \hat{a}_1(t - \tau)}{\sqrt{2}}\right]. \tag{2.62}$$

For the differential mode:

$$\hat{F}_B(t) - \hat{F}_A(t) = 2\frac{\sqrt{2\hbar\omega_0 I_0}}{c}\hat{a}_1(t-\tau). \tag{2.63}$$

This means that the motion of the differential mode under both the radiation-pressure force and the tidal force, $F^h_{A,B} = \mp mL\ddot{h}(t)/2$, from GW is:

$$m\,\ddot{\hat{x}}_d(t) = \hat{F}_B(t) - \hat{F}_A(t) + F^h_B(t) - F^h_A(t) = 2\frac{\sqrt{2\hbar\omega_0 I_0}}{c}\hat{a}_1(t-\tau) + mL\ddot{h}(t). \tag{2.64}$$

Equations (2.59), (2.60) and (2.61) are identical to Eqs. (2.24)–(2.26), if we identify the previous $2\,\hat{x}$ by the differential displacement $\hat{x}_d$ here. Since the GW signal also increases by a factor of 2, due to the differential motion of two arms, the signal strength will not change. Therefore, the signal-referred noise spectrum obtained in the free-space case also applies [cf. Eq. (2.36)], namely:

$$S^h(\Omega) = \left[\frac{1}{\kappa} + \kappa\right]\frac{h^2_{\mathrm{SQL}}}{2}, \tag{2.65}$$

except for the fact that here:

$$\kappa = \frac{4I_0\omega_0}{mc^2\Omega^2}, \quad h_{\mathrm{SQL}} = \sqrt{\frac{4}{m\Omega^2L^2}}. \tag{2.66}$$

2.6.2 *Interferometer With Power-Recycling Mirror and Arm Cavities*

In order to decrease the shot noise, we need to increase the optical power. It would be difficult to achieve a high optical power by solely increasing the input power. Instead, we can add a power-recycling mirror, as first proposed by [13] (see Fig. 2.11). The output optical field from the common port gets coherently reflected back into the interferometer, and amplifies the circulation power. Since we are only concerned with the optical field in the differential port, the effect of the PRM can easily be included by simply replacing the input I_0 in $\hat{E}^{\mathrm{c}}_{\mathrm{in}}(t)$ (Eq. 2.54) by:

$$I_0' \equiv \frac{4}{T_{\mathrm{PRM}}}I_0, \tag{2.67}$$

where T_{PRM} is the power transmissivity of the PRM. Further improvement of the sensitivity comes from the arm cavities formed by the ITMs and ETMs. These cavities are tuned on resonance, further increasing the optical power circulating in the arms, and also coherently amplifying the GW signal by increasing the effective arm length.

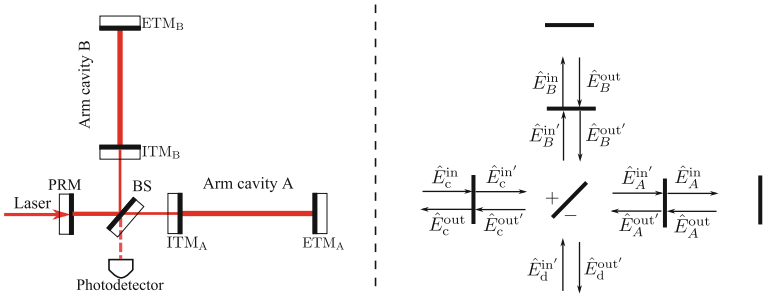

Fig. 2.11 A schematic plot of a Michelson interferometer with a power-recycled mirror (*PRM*) and additional ITMs to form arm cavities (*left*). The corresponding propagating fields are indicated in the *right* diagram

The input–output relation at the differential port also has *the same form as the tuned Fabry-Pérot cavity* discussed in Sect. 2.5.2. This can be shown as follows: The new optical fields $\hat{E}_A^{\rm in'}$ and $\hat{E}_A^{\rm out'}$ are related to $\hat{E}_A^{\rm in}$ and $\hat{E}_A^{\rm out}$ simply by:

$$\hat{E}_A^{\rm in} = \sqrt{R_I}\,\hat{E}_A^{\rm out} + \sqrt{T_I}\,\hat{E}_A^{\rm in'}, \tag{2.68}$$

$$\hat{E}_A^{\rm out'} = \sqrt{T_I}\,\hat{E}_A^{\rm out} - \sqrt{R_I}\,\hat{E}_A^{\rm in'}, \tag{2.69}$$

where $\sqrt{R_I}$ and $\sqrt{T_I}$ are the reflectivity and transmissivity of the ITM, respectively. Similar relations hold for the fields propagating in the arm cavity B. These new fields are connected to the new input $\hat{E}_{\rm c}^{\rm in'}$ and $\hat{E}_{\rm d}^{\rm in'}$ by:

$$\hat{E}_{\rm A,B}^{\rm in'} = \frac{\hat{E}_{\rm c}^{\rm in'}(t) \mp \hat{E}_{\rm d}^{\rm in'}(t)}{\sqrt{2}}. \tag{2.70}$$

In addition, the new output in the differential port is:

$$\hat{E}_{\rm d}^{\rm out'} = \frac{\hat{E}_B^{\rm out'}(t) - \hat{E}_A^{\rm out'}(t)}{\sqrt{2}}. \tag{2.71}$$

The relations between the new inputs $\hat{E}_{\rm d}^{\rm in'}$, $\hat{E}_{\rm d}^{\rm out'}$ and outputs $\hat{E}_{\rm d}^{\rm in}$, $\hat{E}_{\rm d}^{\rm out}$, at the differential port, are simply defined by:

$$\hat{E}_{\rm d}^{\rm in} = \sqrt{R_I}\,\hat{E}_{\rm d}^{\rm out} + \sqrt{T_I}\,\hat{E}_{\rm d}^{\rm in'}, \tag{2.72}$$

$$\hat{E}_{\rm d}^{\rm out'} = \sqrt{T_I}\,\hat{E}_{\rm d}^{\rm out} - \sqrt{R_I}\,\hat{E}_{\rm d}^{\rm in'}. \tag{2.73}$$

These have the same form as Eqs. (2.37) and (2.38). Therefore, as long as we are only concerned with the fields at the differential port, the new input and output are related to the previous ones without arm cavities in a similar way as that of a single

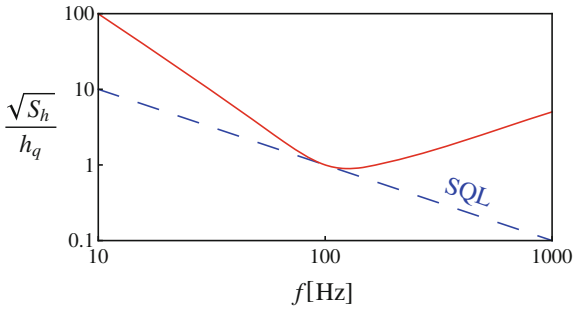

Fig. 2.12 The GW strain-referred sensitivity of an advanced GW detector with power-recycled mirror and arm cavities, given the specifications detailed in the main text. Here, we have normalized the spectrum by h_q, which is defined to be $h_{\rm SQL}$ at 100 Hz

tuned Fabry-Pérot cavity. There is only one difference: in the single tuned cavity analysis, we assumed the front mirror is fixed, while in the GW detector, both ITMs and ETMs can move and the relative motion is detected, which has a reduced mass of $m/2$ in each arm. By further taking into account a factor of two increase in the sensitivity from two arms, the resulting signal-referred noise spectrum reads [cf. Eq. (2.43)]:

$$S^h(\Omega) = \left[\frac{1}{\mathcal{K}} + \mathcal{K}\right] \frac{h_{\rm SQL}^2}{2}, \tag{2.74}$$

with

$$\mathcal{K} \equiv \frac{2\gamma\, \iota_c}{\Omega^2(\Omega^2+\gamma^2)}, \quad h_{\rm SQL} = \sqrt{\frac{8\hbar}{m\Omega^2 L^2}}. \tag{2.75}$$

The cavity bandwidth, $\gamma \equiv T_I c/(4L)$, and the parameter ι_c are the same as in Eq. (2.42), but with $I_c \equiv 8I_0/(T_{\rm PRM}T_I)$, which is enhanced by both the power-recycling and arm cavities. To illustrate this sensitivity, we can choose the following specifications for different parameters (close to those of the AdvLIGO): mass of individual test mass $m = 40$ kg, intra-cavity optical power $I_c = 800$ kW, arm cavity length $L = 4$ km, optical angular frequency $\omega_0 = 1.9 \times 10^{15}{\rm s}^{-1}$ (wavelength equal to 1μm), arm cavity bandwidth $\gamma/(2\pi) = 100$ Hz. The corresponding sensitivity is shown in Fig. 2.12, and it achieves the SQL round 100 Hz.

2.6.3 Interferometer With Signal-Recycling

Now we are ready to analyze the quantum noise in an advanced GW detector with both power- and signal-recycling. The schematic plot of the configuration is shown in Fig. 2.13, where a signal-recycling mirror is added onto the differential port, as first proposed by [17, 23]. After previously introducing all the techniques, the effect on the detector sensitivity also becomes apparent. With the same idea, we can

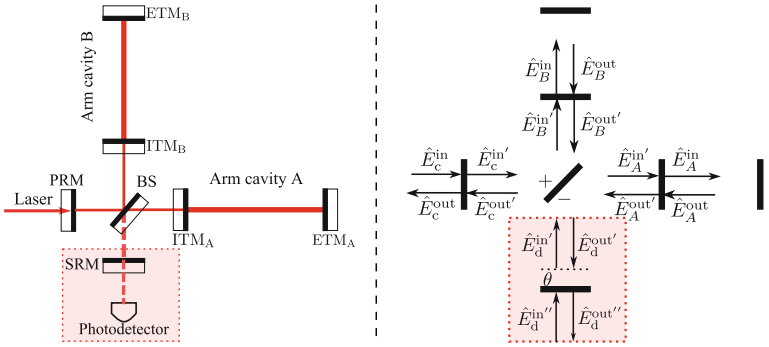

Fig. 2.13 A schematic plot of a Michelson interferometer with a power- (*PRM*) and signal-recycled mirrors (*SRM*) and additional ITMs to form arm cavities (*left*). The corresponding propagating fields are indicated in the *right*-hand diagram, with θ being the detuned phase

relate the new input and output fields $\hat{E}_{\rm d}^{\rm in''}$, $\hat{E}_{\rm d}^{\rm out''}$ to the $\hat{E}_{\rm d}^{\rm in'}$, $\hat{E}_{\rm d}^{\rm out'}$ fields analyzed in the previous section. The relation reads:

$$\hat{E}_{\rm d}^{\rm in'}(t) = \sqrt{R_S}\,\hat{E}_{\rm d}^{\rm out'}(t - 2\theta/\omega_0) + \sqrt{T_S}\,\hat{E}_{\rm d}^{\rm in''}(t - \theta/\omega_0), \tag{2.76}$$

$$\hat{E}_{\rm d}^{\rm out''}(t) = \sqrt{T_S}\,\hat{E}_{\rm d}^{\rm out'}(t - \theta/\omega_0) - \sqrt{R_S}\,\hat{E}_{\rm d}^{\rm in''}(t), \tag{2.77}$$

with θ the detuned phase and R_S and T_S the reflectivity and transmissivity of the SRM, respectively. The corresponding quadratures will undergo rotations identical to those shown in the single detuned cavity analysis [cf. Eqs. (2.45) and (2.46)]. The expression for this input–output relation is very lengthy and complicated [6, 7]. We will follow the approach in Ref. [11] and map the entire signal-recycled interferometer into a single detuned cavity, which will then allow us to directly use the results obtained in Sect. 2.5.3.

The idea behind this mapping is based upon the fact that the length, $L_{\rm SR}$, of the signal-recycling cavity formed by the ITMs and the SRM is, of the order of 10 m, which is very short compared with kilometer long arm cavity. The propagation phase shift of the sidebands around 100 Hz, $e^{i\Omega L_{\rm SR}}$, is negligible [18, 19]. As shown schematically in Fig. 2.14, the signal-recycling cavity can be replaced by one mirror with a set of effective reflectivities and transmissivities, which are related to $T_{S,I}$ and $R_{S,I}$ by:

$$r_{\rm eff} = -\frac{\sqrt{R_S} + \sqrt{R_I}\,e^{2i\theta}}{1 + \sqrt{R_I}e^{2i\theta}}, \quad t'_{\rm eff} = \frac{\sqrt{R_I} + \sqrt{R_S\,R_I}\,e^{2i\theta}}{1 + \sqrt{R_S\,R_I}\,e^{2i\theta}}, \tag{2.78}$$

$$t_{\rm eff} = t'_{\rm eff} = \frac{\sqrt{T_S\,T_I}\,e^{i\theta}}{1 + \sqrt{R_S\,R_I}\,e^{2i\theta}}. \tag{2.79}$$

From the resonant condition of the effective cavity:

Fig. 2.14 Mapping from a three-mirror cavity to a two-mirror cavity by defining the effective transmissivities ($t_{\rm eff}$, $t'_{\rm eff}$) and reflectivities ($r_{\rm eff}$, $r'_{\rm eff}$) of the signal-recycling cavity

$$r'_{\rm eff} e^{2i\Omega_{\rm res}L/c} = 1, \tag{2.80}$$

we can define its effective bandwidth $\gamma_{\rm eff}$ and detuning $\Delta_{\rm eff}$ through:

$$\Omega_{\rm res} \equiv -\Delta_{\rm eff} - i\,\gamma_{\rm eff}. \tag{2.81}$$

Up to the leading order of T_I, $\Delta_{\rm eff}$ and $\gamma_{\rm eff}$ can be expressed in terms of $\sqrt{T_{S,I}}$, $\sqrt{R_{S,I}}$ and θ through

$$\Delta_{\rm eff} = \frac{2\sqrt{R_S}\gamma_I \sin 2\theta}{1 + R_S + 2\sqrt{R_S}\cos 2\theta}, \quad \gamma_{\rm eff} = \frac{(1 - R_S)\gamma_I}{1 + R_S + 2\sqrt{R_S}\cos 2\theta}, \tag{2.82}$$

with the bandwidth of the arm cavity $\gamma_I \equiv c\,T_I/(4L)$.

After this equivalent mapping into a single detuned cavity, it is straightforward to obtain the input–output relation for the signal-recycling interferometer, through the following replacement in Eq. (2.48):

$$\gamma \to \gamma_{\rm eff}, \quad \Delta \to \Delta_{\rm eff}. \tag{2.83}$$

For illustration, we assume an ideal phase-quadrature detection with $\zeta = \pi/2$; the corresponding GW strain-referred sensitivity is given by [cf. Eq. (2.53)]:

$$S^h(\Omega) = \frac{4\gamma_{\rm eff}^2(\iota_c + \Delta_{\rm eff}\Omega^2)^2 + [\Delta_{\rm eff}\iota_c + \Omega^2(\gamma_{\rm eff}^2 - \Delta_{\rm eff}^2 + \Omega^2)]^2}{4\gamma_{\rm eff}\iota_c\Omega^2(\gamma_{\rm eff}^2 + \Omega^2)} h_{\rm SQL}^2. \tag{2.84}$$

One interesting example is when $\theta = \pi/2$, giving

$$\gamma_{\rm eff} = \frac{1 + \sqrt{R_S}}{1 - \sqrt{R_S}}\gamma, \quad \Delta_{\rm eff} = 0. \tag{2.85}$$

The resulting noise spectrum is the same as the previous case without signal-recycling, but with an increased detection bandwidth [a factor of $(1 + \sqrt{R_S})/(1 - \sqrt{R_S})$]. This is the so-called *Resonant-Sideband-Extraction* (RSE) scheme which will be implemented in AdvLIGO. The spectrum is shown in Fig. 2.15. In general, $\theta \neq \pi/2$ and we also show the noise spectrum in the case for a SR cavity detuned phase $\theta = 1.1$. As we can see, there are two minima in the sensitivity curve. Interestingly, they surpass the SQL around the most sensitive frequency ($\sim$100 Hz for

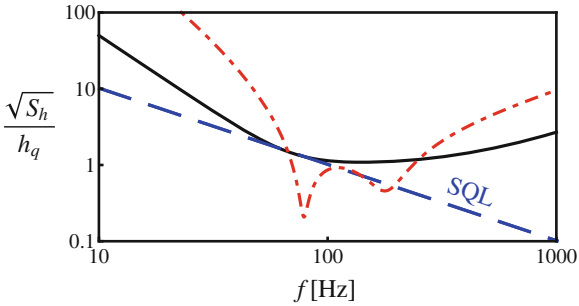

Fig. 2.15 The GW strain-referred sensitivity of a signal-recycling GW detector given a phase-quadrature detection $\zeta = \pi/2$. The *solid* curve corresponds to the RSE scheme with $\theta = \pi/2$ and $\sqrt{R_S} = 0.6$. The *dashed* curve shows the case with $\theta = 1.1$ and $\sqrt{R_S} = 0.9$

given specifications). To gain a better insight into these features which surpasses the SQL, we need to examine the origin of the SQL from a more general picture of linear continuous measurements. Not only will it allow us to understand this particular example, but it can also provide an insight into the SQL, and thus help us to find other approaches to surpass it.

2.7 Derivation of the SQL: A General Argument

Throughout the previous discussions, we have learnt that there are two types of noise, namely shot noise and radiation-pressure noise. They together give rise to the SQL of the detector sensitivity. Actually, the SQL exists in general linear continuous measurements, and it is directly related to the fundamental *Heisenberg Uncertainty Principle* [3]. We will elaborate on this point in this section.

The model of a typical measurement process is shown schematically in Fig. 2.16. The signal—a classical force G (e.g., from the GW) is driving the probe (e.g., the test mass) which is in turn coupled to an external detector (e.g., the optical field). The detector reads out the probe motion by monitoring its displacement $\hat{x}$, and at the same time it exerts a back-action force $\hat{F}$ onto the conjugate momentum of the probe. The signal force G can then be extracted from the detector output $\hat{Y}$, which contains both the signal and the fundamental measurement noise $\hat{Z}$ (i.e., the shot noise). Mathematically, the displacement-referred output $\hat{Y}$, i.e., the measurement result, can be written as:

$$\hat{Y}(t) = \hat{x}_0 + \hat{Z}(t) + \int_{-\infty}^{t} dt' R_{xx}(t - t')[\hat{F}(t') + G(t')]. \tag{2.86}$$

Here $\hat{x}_0$ is the free-evolution value of the probe displacement when the detector is detached, and it has the following two-time commutator:

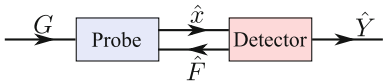

Fig. 2.16 A schematic model of a linear continuous measurement process

$$[\hat{x}_0(t),\ \hat{x}_0(t')] = -i\hbar\, R_{xx}(t-t'), \tag{2.87}$$

where $R_{xx}(t)$ is the response function of the probe to the external force. Here, we require that the detector is tunable, and has a parameter ϵ, with:

$$\hat{Z}_\epsilon(t) = \frac{\epsilon}{\epsilon_0}\hat{Z}_{\epsilon_0}(t), \quad \hat{F}_\epsilon(t) = \frac{\epsilon_0}{\epsilon}\hat{F}_{\epsilon_0}(t). \tag{2.88}$$

The fact that $\hat{Y}(t)$ is the measurement result itself dictates that

$$[\hat{Y}(t), \hat{Y}(t')] = 0, \tag{2.89}$$

because measuring $\hat{Y}(t)$ continuously should not impose any additional noise [3]. In addition, since $\hat{Z}$ and $\hat{F}$ are operators that belong to a different system (the detector) from the probe, they both commute with the probe displacement $\hat{x}_0$. It is therefore required that the two-time commutator of $\hat{Z}$ and $\hat{F}$ terms in $\hat{Y}$ must cancel the commutator from $\hat{x}_0$. In fact, because $\hat{Z}$ and $\hat{F}$ have different scalings in ϵ, and because the cancelation must happen at all orders of ϵ, we can obtain:

$$[\hat{Z}(t),\ \hat{Z}(t')] = [\hat{F}(t),\ \hat{F}(t')] = 0, \quad [\hat{Z}(t),\ \hat{F}(t')] = i\hbar\,\delta(t-t'). \tag{2.90}$$

This indicates that the shot noise and the back-action noise do not commute at the same moment. In the frequency domain, this can be written as:

$$[\hat{Z}(\Omega),\ \hat{Z}(\Omega')] = [\hat{F}(\Omega),\ \hat{F}(\Omega')] = 0, \quad [\hat{Z}(\Omega),\ \hat{F}(\Omega')] = 2\pi\, i\hbar\,\delta(\Omega-\Omega'). \tag{2.91}$$

If we introduce the single-sided (cross) spectral densities $S_{ZZ}(\Omega)$, $S_{FF}(\Omega)$ and $S_{ZF}(\Omega)$, the above commutation relations dictate the Heisenberg Uncertainty Principle:

$$S_{ZZ}(\Omega)S_{FF}(\Omega) - |S_{ZF}(\Omega)|^2 \geq \hbar^2. \tag{2.92}$$

This generally will not set a bound on the noise spectrum in measuring the probe displacement [cf. Eq. (2.86)] which is given by:

$$S^x(\Omega) = S_{ZZ}(\Omega) + 2\Re[R_{xx}(\Omega)\, S_{ZF}(\Omega)] + |R_{xx}(\Omega)|^2 S_{FF}(\Omega) \tag{2.93}$$

with $R_{xx}(\Omega)$ the Fourier transform of $R_{xx}(t)$. However, when there is no correlation between the shot noise and the back-action noise, namely $S_{ZF} = 0$, it induces the SQL for the displacement measurement:

$$S^x(\Omega) \geq 2|R_{xx}(\Omega)|\sqrt{S_{ZZ}(\Omega)S_{FF}(\Omega)} \geq 2\hbar|R_{xx}(\Omega)| \equiv S^x_{\mathrm{SQL}}. \tag{2.94}$$

In the case of GW detection, the external force is the GW tidal force on the test masses and we have $G(t) = mL\ddot{h}(t)$ (m is the reduced mass). Therefore, the SQL for the GW signal-referred sensitivity reads

$$S^h_{\rm SQL} = \frac{2\hbar}{m^2\Omega^4 L^2 |R_{xx}(\Omega)|}. \tag{2.95}$$

For a free mass, $R_{xx}(\Omega) = -1/(m\Omega^2)$; this gives the free-mass SQL:

$$S^h_{\rm SQL} = \frac{2\hbar}{m\Omega^2 L^2}, \tag{2.96}$$

which justifies the order-of-magnitude estimate we obtained in Eq. (2.4).

From the above derivation, we immediately realize that there are two possible approaches to surpassing the free-mass SQL: (1) Creating correlations between the shot noise $\hat{Z}$ and the back-action noise $\hat{F}$ with non-zero S_{ZF}. Correspondingly, the inequality in Eq. (2.94) is not satisfied, and the total noise spectrum will not be bounded by the SQL; (2) Modifying the dynamics of the probe: The free-mass SQL will no longer be relevant if the probe has a different response to the external force than the free mass. In particular, for an oscillator with a resonance frequency ω_m and decay rate γ_m, the response function reads $R_{xx}(\Omega) = 1/[-m(\Omega^2 - \omega_m^2 + i\gamma_m\Omega)]$, and then around resonance frequency:

$$\frac{S^h_{\rm SQL}|_{\rm oscillator}}{S^h_{\rm SQL}|_{\rm free\ mass}} = \frac{\sqrt{(\Omega^2-\omega_m^2)^2+\gamma_m^2\Omega^2}}{\Omega^2}\Big|_{\Omega=\omega_m} = \frac{\gamma_m}{\omega_m}. \tag{2.97}$$

The free-mass SQL can therefore be surpassed by a significant amount of the mechanical quality factor ω_m/γ_m around its resonance frequency. We will explore these two approaches in detail in the next two sections.

2.8 Beating the SQL by Building Correlations

In this section, we will focus on the first approach to beat the SQL, by creating correlations between the shot noise and the back-action noise. This can be achieved by: (i) signal-recycling; (ii) squeezed input; (iii) variational readout. The details of these methods will be discussed.

2.8.1 Signal-Recycling

In the previous section (cf. Sect. 2.6.3), we showed that the signal-recycled interferometer can be mapped into a detuned cavity, in which the amplitude and phase quadratures will rotate and mix with each other. When their fluctuations are reflected

back to the test mass by the signal-recycling mirror, both will contribute to the radiation-pressure noise, similarly for the shot noise, which will have contributions from both fluctuations. Therefore, the shot noise and radiation-pressure noise naturally acquire correlations. In the case of phase-quadrature readout, it can be shown that this correlation is given by [8]:

$$S_{ZF} = \hbar \frac{\Delta_{\rm eff}(\Delta_{\rm eff}^2 + 3\gamma_{\rm eff}^2 - \Omega^2)}{2\gamma_{\rm eff}(\gamma_{\rm eff}^2 + \Omega^2)}. \tag{2.98}$$

This accounts for the two minima in the sensitivity curve, which surpass the SQL, as shown in Fig. 2.15.

2.8.2 Squeezed Input

As pointed out in the pioneering work of [16], a frequency-dependent squeezed input can be used to surpass the SQL; in this case, the shot noise and radiation-pressure noise are naturally correlated as a result of the correlation between the amplitude and phase quadratures of the input squeezed light. To illustrate this point, we will only look at the scheme discussed in Sect. 2.6.2 without a signal-recycling mirror. It can be easily generalized and extended to general schemes. Given a squeezed input, the amplitude and phase quadrature will be transformed according to Eqs. (2.17) and (2.18). As shown in [16], if the squeezing angle ϕ has the following frequency dependence:

$$\phi(\Omega) = -\operatorname{arccot} \mathcal{K}(\Omega), \tag{2.99}$$

the amplitude and phase fluctuations are squeezed at low and high frequencies, respectively, and the noise spectrum will be reduced by a overall squeezing factor of e^{2q}, namely:

$$S_{\rm sqz}^h = e^{-2q}\left[\mathcal{K} + \frac{1}{\mathcal{K}}\right]\frac{h_{\rm SQL}^2}{2}, \tag{2.100}$$

which surpasses the SQL at around the most sensitive frequencies, as indicated in Fig. 2.18 . It is possible to achieve a frequency-dependent squeezing, as prescribed in Eq. (2.99), because different sideband frequencies all represent different degrees of freedom, and therefore squeezing them in different ways is totally allowed. In practice, one must invent the right device that generates such a frequency dependence. This usually implies devices with a certain time scale that is comparable to the detection band of the detector, which is very long compared with usual quantum optical devices (Fig. 2.17).

Kimble et al. invented one such device—a detuned Fabry Pérot cavity. For Fabry-Pérot Michelson interferometers, they showed that a squeezing angle of arctan $\mathcal{K}$ can

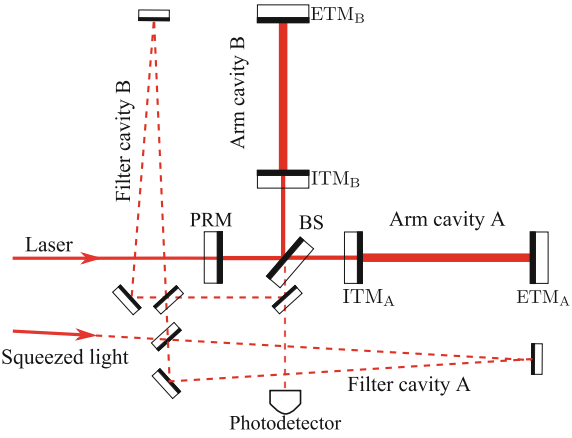

Fig. 2.17 A schematic plot of the frequency-dependent squeezed input configuration. A frequency-independent squeezed light, filtered by two detuned Fabry-Pérot cavities in sequence, produces the required frequency dependence

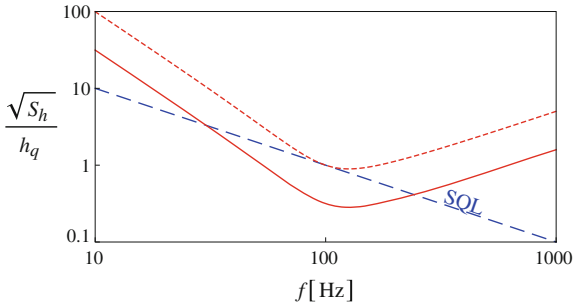

Fig. 2.18 The GW strain-referred sensitivity of a frequency-dependent squeezing input interferometer (*solid curve*). The squeezing factor is $e^{-2q} = 0.1$. The other specification is the same as Fig. 2.12

be generated by feeding a frequency-independent squeezed light into two consecutive Fabry-Pérot cavities, each with a perfect end mirror, and prescribed values of detuning and bandwidth. The specifications for the filter cavity parameters can be obtained by using the technique given in the Appendix of [21]. This technique is valid for general schemes, such as a signal-recycling configuration, shown explicitly in [14], in which the noise spectrum is also reduced by the squeezing factor for the entire detection band.

2.8.3 Variational Readout: Back-Action Evasion

Another natural way to build correlations is to measure a certain combination of the amplitude quadrature $\hat{b}_1$ and phase quadrature $\hat{b}_2$ at the output, namely:

$$\begin{aligned}\hat{b}_\zeta &= \hat{b}_1 \cos\zeta + \hat{b}_2 \sin\zeta \\ &= (\hat{a}_1 \cos\zeta + \hat{a}_2 \sin\zeta) - \hat{a}_1 \mathcal{K} \sin\zeta + \sqrt{2\mathcal{K}} \frac{h}{h_{\mathrm{SQL}}} \sin\zeta .\end{aligned} \tag{2.101}$$

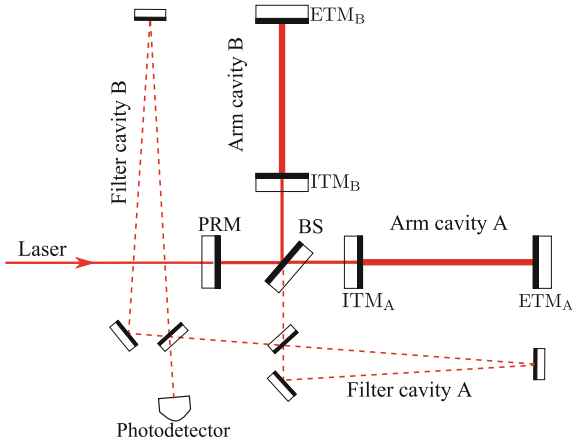

Fig. 2.19 A schematic plot of the variational-readout configuration. The output is filtered by two detuned Fabry-Pérot cavities before the detection

The shot noise $(\hat{a}_1 \cos\zeta + \hat{a}_2 \sin\zeta)$ and the radiation-pressure noise $\hat{a}_1 \mathcal{K} \sin\zeta$ has non-zero correlation. If the detection angle ζ has the following frequency dependence:

$$\zeta(\Omega) = \operatorname{arccot} \mathcal{K}(\Omega), \tag{2.102}$$

we can completely evade the effect of back-action, and obtain a shot-noise only sensitivity, namely:

$$S^h_{\text{var}} = \frac{h^2_{\text{SQL}}}{2\mathcal{K}}. \tag{2.103}$$

Such back-action- evading scheme was first invented by Vyatchanin et al. in a time domain formalism [24, 25], aimed at detecting GWs with known arrival time. The above frequency-domain formalism was developed by Kimble et al., and it is valid for all possible stationary signals. The required frequency dependency can be achieved in a similar way to that of frequency-dependent squeezing, i.e., by filtering the output through detuned Fabry-Pérot cavity, as shown schematically in Fig. 2.19. The specifications for the filter cavities can also be obtained by using the results in Ref. [21]. The corresponding sensitivity curve is shown in Fig. 2.20.

2.8.4 Optical Losses

In the above discussions, we have assumed an ideal lossless situation. However, in reality, there are multiple channels in which losses can be introduced. These include the scattering and losses in the optical elements, and the non-zero transmission of the end mirrors. These optical losses will introduce uncorrelated vacuum fluctuations,

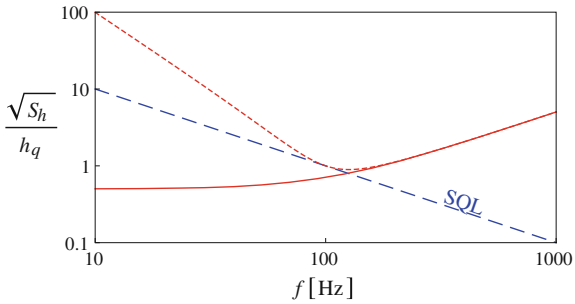

Fig. 2.20 The GW strain-referred sensitivity of a variational-readout scheme (*solid curve*). The low-frequency back-action noise is completed evaded, thus achieving a sensitivity limited only by shot noise

and destroy the quantum coherence. They can be modeled by an overall reduction of the field amplitude by $\sqrt{1-\epsilon}$, and then an introduction of $\sqrt{\epsilon}$ for the vacuum:

$$\vec{b} \to \sqrt{1-\epsilon}\vec{b} + \sqrt{\epsilon}\vec{n}. \tag{2.104}$$

Here $\vec{n}$ is associated with the uncorrelated vacuum fluctuations. They will not only affect the injected squeezed state but also the output field, which undermines the sensitivity. As shown by Kimble et al., the squeezed-input configuration is reasonably robust against optical loss as long as the filter cavities have a length comparable to the arm cavity (∼4 km). However, the variational-readout scheme is very susceptible to the optical losses. If we apply the condition in Eq. (2.102), the noise spectrum with the output loss [cf. Eq. (2.104)] is:

$$S^h_{\rm loss}(\Omega) = \left[\frac{\epsilon}{2(1-\epsilon)\mathcal{K}\sin^2\zeta} + \frac{1}{2\mathcal{K}}\right] h^2_{\rm SQL}. \tag{2.105}$$

At low frequencies, $\mathcal{K} \sim \Omega^{-2}$ and $\sin^2\zeta \sim \Omega^4$, and thus the first term scales as Ω^{-2}. This means that the loss will severely affect the low-frequency sensitivity. In addition, as shown by Kimble et al., around the frequency where the SQL is attained for a conventional scheme without a signal-recycling mirror, the SQL beating ratio of a variational-readout scheme with loss is given by:

$$\mu \equiv \sqrt{\frac{S^h_{\rm SQL}}{S^h_{\rm var}}} \approx \sqrt[4]{\epsilon}, \tag{2.106}$$

only if the interferometer can manage a factor of $1/\sqrt{\epsilon}$ times stronger optical power. Given a typical loss of 0.01, this produces a factor of 0.3 and a power 10 times greater, which is rather challenging. Therefore, a low-loss optical setup is essential for implementation.

2.9 Optical Spring: Modification of Test-Mass Dynamics

Apart from building correlations, as shown by Eq. (2.97), the free-mass SQL can also be surpassed by modifying the dynamics of the test-mass. One might expect that this will require a significant modification of the topology of current GW detectors. As it turns out, a detuned signal-recycling interferometer naturally achieves this. This is intimately connected to the rotation of the amplitude and phase quadrature in the signal-recycling cavity, which produces correlations between the shot noise and radiation-pressure noise. As we have previously mentioned, the radiation pressure force not only depends on the amplitude quadrature, but also on the phase quadrature. Since the latter contains the test-mass displacement, it induces a position-dependent force and modifies the test-mass dynamics; This phenomenon is also called the "optical-spring" effect. A similar idea, but with a different configuration, was first proposed by [19], and is the so-called "optical bar" GW detector.

2.9.1 Qualitative Understanding of Optical-Spring Effect

The optical-spring effect can be understood qualitatively by looking at the case of a single detuned cavity. The displacement of the end mirror (test-mass) x will change the intra-cavity power I_c, which in turn changes the radiation-pressure force. In the adiabatic limit, the intra-cavity power as a function of x reads:

$$I_c(x) = \frac{\gamma^2 I_c^{\max}}{\gamma^2 + [\Delta + (\omega_0 x/L)]^2}, \tag{2.107}$$

which is shown in the left panel of Fig. 2.21. Since the radiation-pressure force is equal to $F(x) = I_c(x)/c$, such a position-dependent force will introduce a rigidity, which is minus the derivative of the force $-dF(x)/dx$, around the equilibrium point $x = 0$. Depending on the sign of the detuning, it will create either negative or positive rigidity. In the case of a detuned signal-recycling configuration for AdvLIGO, a strong optical-spring effect can shift the pendulum frequency of 1 Hz up to the detection band. Around the new resonant frequency, we can surpass the free-mass SQL. This actually accounts for the low-frequency dip in Fig. 2.15. One can refer to Ref. [7] for a detailed discussion of the mechanical resonance due to this optical-spring effect.

Due to a delayed response of the intra-cavity power to the test-mass motion, the optical spring also has a friction component. For $\Delta < 0$, such a delayed response gives a positive damping, which pumps energy out of the test mass. For $\Delta > 0$, the damping is negative, which will destabilize the system. Using the input–output relation derived in Sect. 2.5.3, one can easily determine the expression for an optical spring in the frequency domain as:

$$K(\Omega) = -\frac{2I_c\omega_0}{Lc}\frac{\Delta}{(\Omega - \Delta + i\gamma)(\Omega + \Delta + i\gamma)}. \tag{2.108}$$

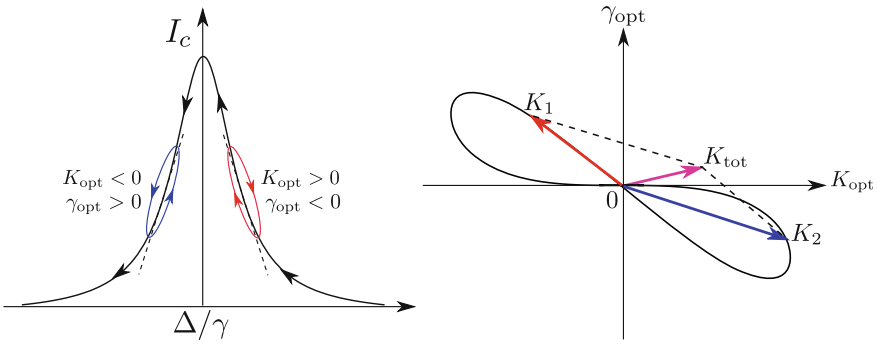

Fig. 2.21 The optical power as a function of cavity detuning Δ (*left*). A double optical spring, $K_{\rm tot}(\Omega) = K_1(\Omega) + K_2(\Omega)$, which has both positive rigidity and damping (*right*). The *black* curve (*right*) shows a parametric plot of the optical spring $K(\Omega)$ as a function of detuning

For sideband frequencies $\Omega < \Delta, \gamma$, we can perform a Taylor expansion and obtain

$$K(\Omega) = \frac{2I_c\omega_0}{Lc}\left[\frac{\Delta}{\gamma^2+\Delta^2} + \frac{2i\gamma\Delta}{(\gamma^2+\Delta^2)^2}\Omega\right] \equiv K_{\rm opt} - i\gamma_{\rm opt}\Omega. \tag{2.109}$$

We have introduced the rigidity $K_{\rm opt}$ (real part of K) and the damping $\gamma_{\rm opt}$ (imaginary part). As we can see, the positive (negative) rigidity is always accompanied by a negative (positive) damping. In either case, the system is unstable. To stabilize the system, one can use a feedback control as described by [6]. An interesting alternative is to implement the idea of a double optical spring, by pumping the cavity with two lasers at different frequencies [12, 22]. One laser with a small detuning provides a large positive damping while another with a large detune, but with a high power, provides a strong restoring force. The resulting system is self-stabilized with both positive rigidity and positive damping, as shown schematically in the right panel of Fig. 2.21.

2.10 Continuous State Demolition: Another Viewpoint on the SQL

In the previous section (cf. Sect. 2.7), we derive the SQL by focusing on the quantum nature of the detection (the optical field). In this section, we will derive the SQL from another perspective—continuous state demolition. This will guide us to finding new approaches to surpassing the SQL.

In the Heisenberg picture, suppose we attempt to measure the position of a free mass successively at discrete times separated by τ. We measure $\hat{x}$ at time t_1, *then right after* t_1, the quantum state of the test mass is characterized by a standard deviation comparable to the individual-measurement error ϵ, or:

$$\Delta x(t_1 + 0) = \epsilon. \tag{2.110}$$

The value of ϵ decreases indefinitely as individual-measurement sensitivity increases. Applying free-mass quantum mechanics for the duration of $t \in (t_1, t_2)$, we have

$$[\hat{x}(t_1 + 0), \hat{x}(t_2 - 0)] = \frac{i\hbar(t_2 - t_1)}{m} = \frac{i\hbar\tau}{m}. \tag{2.111}$$

The decreasing ϵ will lead to an increasing variance in $\Delta x(t_2 - 0)$ right before the second measurement. This is because the Heisenberg Uncertainty Principle dictates that:

$$\Delta x(t_1 + 0) \cdot \Delta x(t_2 - 0) \geq \hbar\tau/(2m), \tag{2.112}$$

and

$$\Delta x(t_2 - 0) > \frac{\hbar\tau}{2m\epsilon}. \tag{2.113}$$

This large variance in the $x(t_2 - 0)$ distribution will be reduced down to ϵ by the subsequent measurement on $x(t_2)$—but at the price of *demolishing* a quantum state with a large spread of $x(t_2)$ into classical superpositions of quantum states with much smaller variances.

If the successive measurements are done without coordination, i.e., if the *meters* that collapse the mirror's states at t_1 and t_2 are not correlated, then the demolition will cause an additional noise, because the new center of the wavefunction after collapse is randomly chosen among a distribution with variance $\Delta x(t_2 - 0)$. If we now characterize the noise of each individual measurement in position, we obtain,

$$\Delta x \geq \max\left(\epsilon, \frac{\hbar\tau}{2m\epsilon}\right) \geq \sqrt{\frac{\hbar\tau}{2m}}. \tag{2.114}$$

This provides us with the scale of the standard quantum limit. In fact, if for any pulse with duration τ, which can vary at all scales, our measurement error is always:

$$\Delta x \sim \sqrt{\frac{\hbar\tau}{2m}}, \tag{2.115}$$

then the *noise spectral density* of the device is characterized by:

$$S^x(\Omega) \sim \frac{\hbar}{2m\Omega^2}. \tag{2.116}$$

Therefore, the SQL can be traced back to the fact that the test mass positions at different times do not commute with themselves [cf. Eq. (2.111)].

2.11 Speed Meters

This alternative viewpoint on the SQL naturally brings us to the idea of a speed meter, which measures the speed (momentum) instead of the position of the test mass. Since the momentum of a free mass is a conserved dynamical quantity, and its Heisenberg operators at different times commute with each other, one can measure it continuously without imposing additional noise, thus allowing us to surpass the SQL.

Apart from beating the SQL, other more practical issues that make the speed meter attractive are the following: (1) the previous schemes require frequency-dependent squeezing or readout which has led to the requirement of two extra kilometer-scale filter cavities—a high cost in practical construction; (2) the high value of $\mathcal{K}$ at low frequencies leads to a strong sensitivity to optical losses. As it turns out, these issues are resolved simultaneously when we try to build a speed meter, which has a constant sensitivity to the speed of test masses in low frequencies—the requirement for frequency dependence on squeezing and readout quadrature therefore vanishes. In fact, if we imagine an interferometer with a constant κ [cf. Eq. (2.29)] or $\mathcal{K}$ [cf. Eq. (2.41)] in the input–output relation, it will indeed respond to the speed of the mirror.

Here we will discuss two realizations, both found as prototypes in the early papers of [5, 15], but later gradually deformed into the shape of kilometer-scale laser interferometers [11, 20, 21].

2.11.1 Realization I: Coupled Cavities

A possible Michelson variant is shown in Fig. 2.22. An additional sloshing cavity is added after the interferometer output. It has an input-mirror with transmissivity T_s and a totally-reflected end mirror. There is another extraction mirror (with a transmissivity of T_0) between the interferometer output and the sloshing cavity, through which we read out the signal. This configuration emerges from the two-resonator model of Braginsky and Khalili, where it was pointed out that if two resonators are coupled, then a sloshing of signal light between the two cavities cancel each other out, leaving only a sensitivity to the change in mirror position, i.e., the speed. The characteristic sloshing frequency is given by:

$$\omega_s = \frac{\sqrt{T_s}c}{2L}. \tag{2.117}$$

The explicit expression for the response function of the output to the test mass motion can be found by analyzing the input–output relation, giving:

$$\mathcal{T}(\Omega) = \frac{\omega_0}{L}\frac{i\Omega}{\Omega^2 - \omega_s^2 + i\gamma\Omega}, \tag{2.118}$$

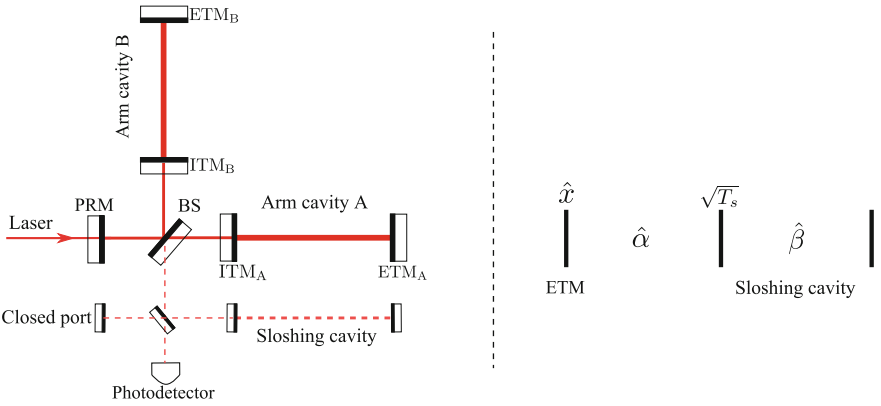

Fig. 2.22 A schematic plot of a speed-meter configuration with coupled cavities. A sloshing cavity is added after the *dark* port. Such a configuration can be mapped into a three-mirror cavity as schematically shown in the *right*-hand panel, forming a pair of coupled cavities

with $\gamma \equiv 4T_0 c/L$ due to the extraction mirror. This can also be derived by fitting the speed meter into the two-resonator model. We can map the speed meter configuration into a three-mirror cavity, as shown schematically in Fig. 2.22. The '$\hat{x}$' corresponds to the differential motion of the end test masses. The left cavity corresponds to the power-recycled Michelson interferometer, and the right cavity is still the sloshing cavity. The optical fields are summarized by two cavity modes $\hat{\alpha}$ and $\hat{\beta}$. Their equations of motion are:

$$\dot{\hat{\alpha}}(t) + \gamma\,\hat{\alpha}(t) = i\omega_s\,\hat{\beta}(t) + i\frac{\omega_0}{L}\hat{x}(t), \tag{2.119}$$

$$\dot{\hat{\beta}}(t) = i\omega_s\,\hat{\alpha}(t). \tag{2.120}$$

We have assumed that both cavity modes are on resonance with respect to the carrier laser frequency. In addition, we attribute the decay only to the left cavity (due to the extraction mirror). The coupling between the two modes is manifested by the sloshing terms on the right hand side (proportional to ω_s). Solving the above equation in the frequency domain will immediately give the result in Eq. (2.118).

The GW strain sensitivity of such a configuration can be derived by using the input–output formalism that we have introduced. Given a frequency-independent squeezing (phase squeezing factor e^{-2q}), the result is (refer to Ref. [21] for more details):

$$S^h = \left[\frac{e^{-2q}}{2\mathcal{K}_{\rm sm}} + \frac{e^{2q}(\cot\zeta - \mathcal{K}_{\rm sm})^2}{2\mathcal{K}_{\rm sm}}\right] h^2_{\rm SQL}, \tag{2.121}$$

where ζ is the readout quadrature angle, and

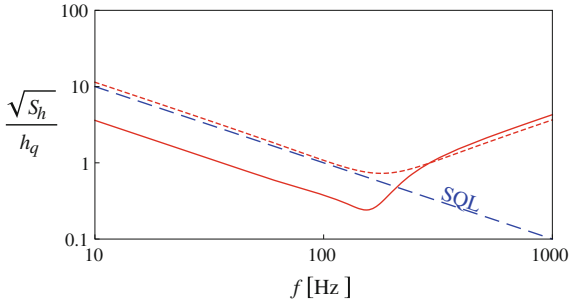

Fig. 2.23 The GW strain-referred sensitivity of the speed meter scheme shown in Fig. 2.22. We have chosen $\gamma/2\pi = 210\,\mathrm{Hz}$, $\omega_s/2\pi = 180\,\mathrm{Hz}$ and $I_c = 800\,\mathrm{kW}$. The *dotted* curve is the case without a phase-squeezed input, and the *solid* curve has $e^{-2q} = 0.1$ (a 10 dB squeezing)

$$\mathcal{K}_{\mathrm{sm}} = \frac{16\omega_0\gamma I_c}{mcL[(\Omega^2-\omega_s^2)^2+\gamma^2\Omega^2]}. \tag{2.122}$$

The first term in S^h is the shot-noise term, and the second is the radiation-pressure noise. At low frequencies, $\mathcal{K}_{\mathrm{sm}}$ is almost a constant. By choosing $\cot\zeta = \mathcal{K}_{\mathrm{sm}}(0)$, the low-frequency radiation-pressure (back-action) can be completely evaded. We show the resulting GW strain sensitivity in Fig. 2.23.

There is, however, a subtle issue: the original Braginsky and Khalili argument stated that momentum can be measured without additional noise—yet in speed meters, we still need back-action evasion: is this still consistent? The answer is yes, because when speed is coupled to an external observable, it ceases to be proportional to the conserved, canonical momentum. Here, we sketch a mathematical proof by Khalili. Suppose the Lagrangian is:

$$\mathcal{L} = \frac{1}{2}m\dot{x}^2 + \alpha\dot{a}_1 x, \tag{2.123}$$

which is the model of a speed meter: the time derivative of the external observable a_1 represents the sloshing. Here, the quantity α is a coupling constant. This is equivalent to:

$$\mathcal{L} = \frac{1}{2}m\dot{x}^2 - \alpha a_1\dot{x}, \tag{2.124}$$

where the coupling becomes a speed coupling, but the canonical momentum is given by:

$$p = \frac{\partial\mathcal{L}}{\partial\dot{x}} = m\dot{x} - \alpha a_1, \tag{2.125}$$

which is conserved, but differs from the kinetic momentum, $m\dot{x}$. This means that a meter that measures speed must add a constant $\alpha a_1/m$, in order to evade the back-action. Note that this is a constant combination between the output phase quadrature

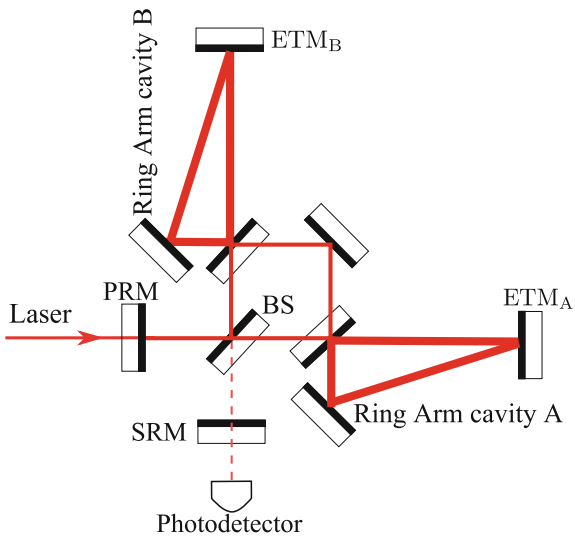

Fig. 2.24 A schematic plot of a Sagnac-type speed meter configuration

and amplitude quadrature—therefore, back-action evasion is straightforward without requiring additional filtering. This is manifested by the fact that $\mathcal{K}_{\rm sm}$ is almost constant at low frequencies.

2.11.2 Realization II: Zero-Area Sagnac

Another possible speed meter configuration is a zero-area Sagnac interferometer, which is shown schematically in Fig. 2.24. This has a different optical topology from the Michelson scheme, where the light travels through two opposite loops in the interferometer. To understand its response to the test-mass motion, we can look at a single trip. The light propagating towards arm A first picks up a phase shift proportional to $ETM_{\rm A}$, displacement $\hat{x}_A(t)$, and it accumulates another phase shift due to motion of $ETM_{\rm B}$, but at $t-\tau$ (τ is the delay time). A similar situation holds for the light propagating towards arm B, but with the roles of $ETM_{\rm A}$ and $ETM_{\rm B}$ swapped. When they recombine at the beam splitter, the total phase shift is simply:

$$\phi_{\rm tot}(t) \propto \hat{x}_A(t) + \hat{x}_B(t-\tau) - \hat{x}_B(t) - \hat{x}_A(t-\tau) \approx [\dot{\hat{x}}_A(t) - \dot{\hat{x}}_B(t)]\tau. \quad (2.126)$$

It naturally has no response to a static change in arm length, but only to the differential speed of the two test masses. Therefore, it is a natural speed meter. This has been recognized by the GW community, but connection with the "Quantum Nondemolition" (QND) speed meter, has never been made. As shown in [25], the GW strain sensitivity of such a configuration is identical to the previous coupled-cavities configuration.

2.12 Conclusions

We have introduced the basic concepts for studying the quantum dynamics and associated quantum noise of an interferometric GW detector. Different insights into the origin of the SQL allow us to find out possible approaches towards surpassing it. In particular, we have considered modifying the input/ouput optics using either frequency-dependent squeezing or a variational readout, and modifying the test mass dynamics through the optical spring effect; and measuring a QND observable of the test mass by using a speed meter. This not only serves as a review of advanced configurations for future GW detectors, but it additionally provides valid examples to help clarify many subtle issues in continuous quantum measurement.

References

1. K.J. Blow, R. Loudon, S.J.D. Phoenix, T.J. Shepherd, Continuum fields in quantum optics. Phys. Rev. A **42**, 4102 (1990)
2. V.B. Braginsky, Classical and Quantum Restrictions on the Detection of Weak Disturbances of a Macroscopic Oscillator. JETP **26**, 831 (1968)
3. V.B. Braginsky, F.Y. Khalili, *Quantum Measurement* (Cambridge University Press, Cambridge, 1992)
4. V.B. Braginsky, M.L. Gorodetsky, F.Y. Khalili, Optical bars in gravitational wave antennas. Phys. Lett. A **232**, 340 (1997)
5. V.B. Braginsky, M.L. Gorodetsky, F.Y. Khalili, K.S. Thorne, Noise in gravitational-wave detectors and other classical-force measurements is not influenced by test-mass quantization. Phys. Rev. D **61**, 044002 (2000)
6. A. Buonanno, Y. Chen, Quantum noise in second generation, signalrecycled laser interferometric gravitational-wave detectors. Phys. Rev. D **64**, 042006 (2001)
7. A. Buonanno, Y. Chen, Signal recycled laser-interferometer gravitational-wave detectors as optical springs. Phys. Rev. D **65**, 042001 (2002)
8. A. Buonanno, Y. Chen, Scaling law in signal recycled laserinterferometer gravitational-wave detectors. Phys. Rev. D **67**, 062002 (2003)
9. C.M. Caves, B.L. Schumaker, New formalism for two-photon quantum optics. I - Quadrature phases and squeezed states. II - Mathematical foundation and compact notation. Phys. Rev. A **31**, 3068 (1985)
10. C.M. Caves, K.S. Thorne, R.W. Drever, V.D. Sandberg, M. Zimmermann, On the measurement of a weak classical force coupled to a quantummechanical oscillator. I. Issues of principle. Rev. Mod. Phys. **52**, 341 (1980)
11. Y. Chen, Sagnac interferometer as a speed-meter-type, quantumnondemolition gravitational-wave detector. Phys. Rev. D **67**, 122004 (2003)
12. T. Corbitt , Y. Chen, E. Innerhofer, H. Mueller-Ebhardt, D. Ottaway, H. Rehbein, D. Sigg, S. Whitcomb, C. Wipf, N. Mavalvala, An All-Optical Trap for a Gram-Scale Mirror. Phys. Rev. Lett. **98**, 150802–150804 (2007)
13. R.W.P. Drever, *Gravitational Radiation* (North-Holland, Amsterdam, 1983)
14. J. Harms, Y. Chen, S. Chelkowski, A. Franzen, H. Vahlbruch, K. Danzmann, R. Schnabel, Squeezed-input, optical-spring, signal-recycled gravitational-wave detectors. Phys. Rev. D **68**, 042001 (2003)

15. F.Y. Khalili, Y. Levin, Speed meter as a quantum nondemolition measuring device for force. Phys. Rev. D **54**, 004735 (1996)
16. H.J. Kimble, Y. Levin, A.B. Matsko, K.S. Thorne, S.P. Vyatchanin, Conversion of conventional gravitational-wave interferometers into quantum nondemolition interferometers by modifying their input and/or output optics. Phys. Rev. D **65**, 022002 (2001)
17. B.J. Meers, Recycling in laser-interferometric gravitational-wave detectors. Phys. Rev. D **38**, 2317 (1988)
18. J. Mizuno, Comparison of Optical Configurations for Laser-Interferometric Gravitational-Wave Detectors. PhD thesis, Max-Planck Institut für Quantenoptik, Garching, Germany, 1995
19. J. Mizuno, K.A. Strain, P.G. Nelson, J.M. Chen, R. Schilling, A. Rüdiger, W. Winkler, K. Danzmann, Resonant sideband extraction: a new configuration for interferometric gravitational wave detectors. Phys. Lett. A **175**, 273 (1993)
20. P. Purdue, Analysis of a quantum nondemolition speed-meter interferometer. Phys. Rev. D **66**, 022001 (2002)
21. P. Purdue, Y. Chen, Practical speed meter designs for quantum nondemolition gravitational-wave interferometers. Phys. Rev. D **66**, 122004 (2002)
22. H. Rehbein, H. Müller-Ebhardt, K. Somiya, S.L. Danilishin, R. Schnabel, K. Danzmann, Y. Chen, Double optical spring enhancement for gravitational-wave detectors. Phys. Rev. D **78**, 062003 (2008)
23. J.Y. Vinet, B. Meers, C. Man, A. Brillet, Optimization of long-baseline optical interferometers for gravitational-wave detection. Phys. Rev. D **38**, 433 (1988)
24. S.P. Vyatchanin, A.B. Matsko, Quantum limit on force measurements. JETP **77**, 218 (1993)
25. S.P. Vyatchanin, E.A. Zubova, Quantum variation measurement of a force. Phys. Lett. A **201**, 269–274 (1995)

http://www.springer.com/978-3-642-25639-4

Exploring Macroscopic Quantum Mechanics in Optomechanical Devices

Miao, H.

2012, XXII, 206 p., Hardcover
ISBN: 978-3-642-25639-4